

Structure of diopside, enstatite, and magnesium aluminosilicate glasses: A joint approach using neutron and x-ray diffraction and solid-state NMR ^{EP}

Cite as: J. Chem. Phys. **157**, 214503 (2022); <https://doi.org/10.1063/5.0125879>

Submitted: 14 September 2022 • Accepted: 04 November 2022 • Published Online: 02 December 2022

Published open access through an agreement with JISC Collections

 Hesameddin Mohammadi,  Rita Mendes Da Silva,  Anita Zeidler, et al.

COLLECTIONS

 This paper was selected as an Editor's Pick



View Online



Export Citation



CrossMark

ARTICLES YOU MAY BE INTERESTED IN

[Structure of molten NaCl and the decay of the pair-correlations](#)

The Journal of Chemical Physics **157**, 094504 (2022); <https://doi.org/10.1063/5.0107620>

[Virial equation of state as a new frontier for computational chemistry](#)

The Journal of Chemical Physics **157**, 190901 (2022); <https://doi.org/10.1063/5.0113730>

[Structure of crystalline and amorphous materials in the NASICON system](#)

$\text{Na}_{1+x}\text{Al}_x\text{Ge}_{2-x}(\text{PO}_4)_3$

The Journal of Chemical Physics **155**, 074501 (2021); <https://doi.org/10.1063/5.0049399>

[Learn More](#)

The Journal of Chemical Physics **Special Topics** Open for Submissions

Structure of diopside, enstatite, and magnesium aluminosilicate glasses: A joint approach using neutron and x-ray diffraction and solid-state NMR

Cite as: J. Chem. Phys. 157, 214503 (2022); doi: 10.1063/5.0125879

Submitted: 14 September 2022 • Accepted: 4 November 2022 •

Published Online: 2 December 2022


















View Online



Export Citation



CrossMark

Hesameddin Mohammadi,¹  Rita Mendes Da Silva,¹  Anita Zeidler,¹  Lawrence V. D. Gammond,¹  Florian Gehlhaar,^{2,3}  Marcos de Oliveira, Jr.,⁴  Hugo Damasceno,⁴  Hellmut Eckert,^{4,5}  Randall E. Youngman,⁶  Bruce G. Aitken,⁶  Henry E. Fischer,²  Holger Kohlmann,³  Laurent Cormier,⁷  Chris J. Benmore,⁸  and Philip S. Salmon^{1,a)} 

AFFILIATIONS

¹ Department of Physics, University of Bath, Bath BA2 7AY, United Kingdom

² Institut Laue Langevin, 71 Avenue des Martyrs, 38042 Grenoble Cedex 9, France

³ Institut für Anorganische Chemie, Universität Leipzig, Johannisallee 29, 04103 Leipzig, Germany

⁴ Instituto de Física de São Carlos, Universidade de São Paulo, CP 369, São Carlos SP 13566-590, SP, Brazil

⁵ Institut für Physikalische Chemie, WWU Münster, Corrensstraße 30, D48149 Münster, Germany

⁶ Science and Technology Division, Corning Incorporated, Corning, New York 14831, USA

⁷ Institut de Minéralogie, de Physique des Matériaux et de Cosmochimie (IMPMC), Sorbonne Université, CNRS UMR 7590, Muséum National d'Histoire Naturelle, IRD UMR 206, 4 place Jussieu, 75005 Paris, France

⁸ X-Ray Science Division, Advanced Photon Source, Argonne National Laboratory, 9700 South Cass Avenue, Lemont, Illinois 60439, USA

^{a)} Author to whom correspondence should be addressed: p.s.salmon@bath.ac.uk

ABSTRACT

Neutron diffraction with magnesium isotope substitution, high energy x-ray diffraction, and ²⁹Si, ²⁷Al, and ²⁵Mg solid-state nuclear magnetic resonance (NMR) spectroscopy were used to measure the structure of glassy diopside (CaMgSi₂O₆), enstatite (MgSiO₃), and four (MgO)_x(Al₂O₃)_y(SiO₂)_{1-x-y} glasses, with $x = 0.375$ or 0.25 along the 50 mol. % silica tie-line ($1 - x - y = 0.5$) or with $x = 0.3$ or 0.2 along the 60 mol. % silica tie-line ($1 - x - y = 0.6$). The bound coherent neutron scattering length of the isotope ²⁵Mg was remeasured, and the value of 3.720(12) fm was obtained from a Rietveld refinement of the powder diffraction patterns measured for crystalline ²⁵MgO. The diffraction results for the glasses show a broad asymmetric distribution of Mg–O nearest-neighbors with a coordination number of 4.40(4) and 4.46(4) for the diopside and enstatite glasses, respectively. As magnesia is replaced by alumina along a tie-line with 50 or 60 mol. % silica, the Mg–O coordination number increases with the weighted bond distance as less Mg²⁺ ions adopt a network-modifying role and more of these ions adopt a predominantly charge-compensating role. ²⁵Mg magic angle spinning (MAS) NMR results could not resolve the different coordination environments of Mg²⁺ under the employed field strength (14.1 T) and spinning rate (20 kHz). The results emphasize the power of neutron diffraction with isotope substitution to provide unambiguous site-specific information on the coordination environment of magnesium in disordered materials.

© 2022 Author(s). All article content, except where otherwise noted, is licensed under a Creative Commons Attribution (CC BY) license (<http://creativecommons.org/licenses/by/4.0/>). <https://doi.org/10.1063/5.0125879>

I. INTRODUCTION

Magnesium is an enigmatic element within network-forming oxide glasses. It can adopt a variety of different local environments, where Mg–O coordination numbers in the range from four to six or more are found in the structural chemistry of its crystalline oxides,^{1–6} and there is debate about the structural role played by four-coordinated magnesium as it is sometimes regarded as a network-forming species.⁷ Definitive experimental information on the coordination environment of Mg²⁺ and its dependence on the glass composition is therefore desirable in order to clarify the structural role of magnesium in disordered network structures. Such information is, however, scarce because of (i) the chameleon-like nature of the magnesium coordination environment, (ii) limitations in x-ray scattering experiments that originate from the low atomic number of magnesium, and (iii) difficulty in interpreting the results obtained from ²⁵Mg solid-state nuclear magnetic resonance (NMR) experiments.⁸ This isotope of magnesium has the only NMR active nucleus, but its natural abundance is small (10%) and the nucleus of this isotope has a low gyromagnetic ratio and significant quadrupolar moment (nuclear spin $I = 5/2$).⁹

In this paper, we investigate the structure of the diopside and enstatite composition glasses (CaO)_{0.25}(MgO)_{0.25}(SiO₂)_{0.5} and (MgO)_{0.5}(SiO₂)_{0.5}, respectively, along with four magnesium aluminosilicate (MgAS) glasses (MgO)_x(Al₂O₃)_y(SiO₂)_{1-x-y}, with $x = 0.375$ or 0.25 along the 50 mol. % silica tie-line ($1 - x - y = 0.5$), or with $x = 0.3$ or 0.2 along the 60 mol. % silica tie-line ($1 - x - y = 0.6$). The latter correspond to glass compositions for which the ratio $R = x/y$ is either three or unity, respectively. These glasses were chosen for investigation because they cover a range of compositions where the role of Mg²⁺ is expected to change from a network modifying ($R \rightarrow \infty$) to a predominantly charge-compensating ($R = 1$) role. They also serve as model systems for technological materials such as commercial display glass^{10,11} and magmatic materials of interest in the geosciences.^{12–15}

The glass structure was probed by combining neutron diffraction with magnesium isotope substitution,¹⁶ high energy x-ray diffraction, and ²⁹Si, ²⁷Al, and ²⁵Mg solid-state NMR spectroscopy. The diffraction and NMR experiments were performed on the same set of samples. The neutron diffraction method was selected because it is designed to deliver unambiguous site-specific structural information.¹⁷ The experiments pointed, however, to a systematic error in the published value for the bound coherent neutron scattering length of the isotope ²⁵Mg.¹⁸ This parameter was therefore remeasured in neutron powder diffraction experiments on isotopically enriched crystalline ²⁵MgO. The requirement in the neutron diffraction work of isotopically enriched samples helped to motivate a reassessment of solid-state ²⁵Mg NMR for delivering unambiguous information on the coordination environment of magnesium in glass.

This paper is organized as follows. The essential diffraction theory is given in Sec. II and the experimental methods are described in Sec. III. The results are presented in Sec. IV and are discussed in Sec. V. Conclusions are drawn in Sec. VI.

II. THEORY

A. Bragg powder diffraction

In a diffraction experiment on a powdered crystalline sample, kinematic theory shows that the intensity of elastically scattered neutrons is given by¹⁹

$$I(2\theta) \propto |F_{hkl}|^2 = \left| \sum_j b_j \text{SOF}_j e^{-i2\pi(hx_j + ky_j + lz_j)} \right|^2, \quad (1)$$

where 2θ is the scattering angle, F_{hkl} is the structure factor for the Miller indices h, k, l , the fractional coordinates x_j, y_j, z_j give the site of atom j within a unit cell, b_j is the coherent neutron scattering length of atom j , and SOF_j is the site occupation factor. For crystalline MgO, which has the NaCl structure type, the fractional coordinates for Mg (0, 0, 0) and O ($1/2, 1/2, 1/2$) are known from its space group $Fm\bar{3}m$, and $\text{SOF}_j = 1$ for both sites because of the well-defined 1:1 stoichiometry of the oxide.² Hence, if b_O is known accurately but there is uncertainty associated with the value for magnesium $b_{\text{Mg}}^{\text{trial}}$, a Rietveld refinement of the measured diffraction pattern with fixed scattering lengths will deliver a fitted value $\text{SOF}_{\text{Mg}}^{\text{fit}} \neq 1$. The correct value for the magnesium scattering length follows from the expression $\tilde{b}_{\text{Mg}} = b_{\text{Mg}}^{\text{trial}} \times \text{SOF}_{\text{Mg}}^{\text{fit}}$, where the tilde indicates that the value will be sensitive to the isotopic enrichment.

B. Pair-distribution function analysis

In a neutron diffraction experiment, the measured total structure factor is given by¹⁷

$$F_N(k) = \sum_{\alpha} \sum_{\beta} c_{\alpha} c_{\beta} b_{\alpha} b_{\beta} [S_{\alpha\beta}(k) - 1], \quad (2)$$

where k is the magnitude of the scattering vector, c_{α} is the atomic fraction of chemical species α , b_{α} is the bound coherent neutron scattering length of chemical species α , and $S_{\alpha\beta}(k)$ is the Faber–Ziman partial structure factor for the chemical species α and β . In an x-ray diffraction experiment, the scattering lengths b_{α} in Eq. (2) are replaced by the k -dependent form factors $f_{\alpha}(k)$ and the total structure factor is usually rewritten as

$$S_X(k) = 1 + F_X(k) / \langle f(k) \rangle^2, \quad (3)$$

where the mean value $\langle f(k) \rangle = \sum_{\alpha} c_{\alpha} f_{\alpha}(k)$. Neutral atom form factors were used in the x-ray diffraction data analysis.²⁰

Let neutron diffraction experiments be performed on two glasses that are identical in every respect, except that one contains magnesium of natural isotopic abundance, ^{nat}Mg, and the other is isotopically enriched with ²⁵Mg. If the measured total structure factors are denoted by ^{nat} $F_N(k)$ and ²⁵ $F_N(k)$, respectively, then the difference function

$$\begin{aligned} \Delta F_{\text{Mg}}(k) &= {}^{\text{nat}}F_{\text{N}}(k) - {}^{25}\text{Mg}F_{\text{N}}(k) \\ &= 2c_{\text{Mg}}\Delta b_{\text{Mg}} \sum_{\alpha \neq \text{Mg}} c_{\alpha}b_{\alpha} [S_{\text{Mg}\alpha}(k) - 1] \\ &\quad + c_{\text{Mg}}^2 (b_{\text{natMg}}^2 - b_{25\text{Mg}}^2) [S_{\text{MgMg}}(k) - 1], \end{aligned} \quad (4)$$

where $\Delta b_{\text{Mg}} = b_{\text{natMg}} - b_{25\text{Mg}}$, eliminates all those pair-correlation functions that do not involve magnesium. The Mg- α correlations with $\alpha \neq \text{Mg}$ can also be eliminated by forming the difference function given by

$$\begin{aligned} \Delta F(k) &= [b_{\text{natMg}} {}^{25}\text{Mg}F_{\text{N}}(k) - b_{25\text{Mg}} {}^{\text{nat}}F_{\text{N}}(k)] / \Delta b_{\text{Mg}} \\ &= \sum_{\alpha \neq \text{Mg}} \sum_{\beta \neq \text{Mg}} c_{\alpha}c_{\beta}b_{\alpha}b_{\beta} [S_{\alpha\beta}(k) - 1] \\ &\quad - c_{\text{Mg}}^2 b_{\text{natMg}} b_{25\text{Mg}} [S_{\text{MgMg}}(k) - 1]. \end{aligned} \quad (5)$$

The difference functions $\Delta F_{\text{Mg}}(k)$ and $\Delta F(k)$ therefore simplify the complexity of correlations associated with a single total structure factor.

The real-space functions corresponding to $F_{\text{N}}(k)$, $\Delta F_{\text{Mg}}(k)$, and $\Delta F(k)$ are obtained by Fourier transformation and are denoted by $D_{\text{N}}(r)$, $\Delta D_{\text{Mg}}(r)$, and $\Delta D(r)$, respectively, where r is a distance in real space. For example, the total pair-distribution function is given by

$$\begin{aligned} D'_{\text{N}}(r) &= \frac{2}{\pi} \int_0^{\infty} dk k [F_{\text{N}}(k) / \langle b \rangle^2] M(k) \sin(kr) \\ &= D_{\text{N}}(r) \otimes M(r), \end{aligned} \quad (6)$$

where the normalization factor $\langle b \rangle^2 = (\sum_{\alpha} c_{\alpha}b_{\alpha})^2$ is obtained by taking the modulus of Eq. (2) after setting all the $S_{\alpha\beta}(k)$ functions to zero and \otimes is the one-dimensional convolution operator. $M(k)$ is a window function given by $M(k) = 1$ for $k \leq k_{\text{max}}$ and $M(k) = 0$ for $k > k_{\text{max}}$, where k_{max} is the maximum k -value and $M(r)$ is the real-space manifestation of $M(k)$. If k_{max} is sufficiently large that $M(k)$ does not truncate oscillations in $F_{\text{N}}(k)$, Eq. (6) will deliver the unmodified total pair-distribution function

$$D_{\text{N}}(r) = \frac{4\pi\rho r}{\langle b \rangle^2} \sum_{\alpha} \sum_{\beta} c_{\alpha}c_{\beta}b_{\alpha}b_{\beta} [g_{\alpha\beta}(r) - 1], \quad (7)$$

where ρ is the atomic number density and $g_{\alpha\beta}(r)$ is the partial pair-distribution function for the chemical species α and β . Similarly,

$$\Delta D'_{\text{Mg}}(r) = \Delta D_{\text{Mg}}(r) \otimes M(r), \quad (8)$$

where

$$\begin{aligned} \Delta D_{\text{Mg}}(r) &= \frac{4\pi\rho r}{B} \left\{ 2c_{\text{Mg}}\Delta b_{\text{Mg}} \sum_{\alpha \neq \text{Mg}} c_{\alpha}b_{\alpha} [g_{\text{Mg}\alpha}(r) - 1] \right. \\ &\quad \left. + c_{\text{Mg}}^2 (b_{\text{natMg}}^2 - b_{25\text{Mg}}^2) [g_{\text{MgMg}}(r) - 1] \right\} \end{aligned} \quad (9)$$

and the normalization factor B is obtained by taking the modulus of Eq. (4) after setting all the $S_{\alpha\beta}(k)$ functions to zero. It follows that, if

the first peak in $\Delta D_{\text{Mg}}(r)$ is attributable to Mg-O correlations alone, then the Mg-O coordination number can be obtained from

$$\tilde{n}_{\text{Mg}}^{\text{O}} = \frac{B}{2c_{\text{Mg}}\Delta b_{\text{Mg}}b_{\text{O}}} \int_{r_1}^{r_2} dr r [\Delta D'_{\text{Mg}}(r) + 4\pi\rho r] \quad (10)$$

where r_1 and r_2 give the lower and upper boundaries of the peak, respectively. In addition

$$\Delta D'(r) = \Delta D(r) \otimes M(r), \quad (11)$$

where

$$\begin{aligned} \Delta D(r) &= \frac{4\pi\rho r}{C} \left\{ \sum_{\alpha \neq \text{Mg}} \sum_{\beta \neq \text{Mg}} c_{\alpha}c_{\beta}b_{\alpha}b_{\beta} [g_{\alpha\beta}(r) - 1] \right. \\ &\quad \left. - c_{\text{Mg}}^2 b_{\text{natMg}} b_{25\text{Mg}} [g_{\text{MgMg}}(r) - 1] \right\} \end{aligned} \quad (12)$$

and the normalization factor C is obtained by taking the modulus of Eq. (5) after setting all the $S_{\alpha\beta}(k)$ functions to zero.

At r -values below the distance of closest approach between two atoms of chemical species α and β , the partial pair-distribution function $g_{\alpha\beta}(r) = 0$. It follows that, at these small r -values, $D_{\text{N}}(r) = \Delta D_{\text{Mg}}(r) = \Delta D(r) = -4\pi\rho r$, i.e., all three functions follow the so-called density line. Provided the datasets have been correctly normalized, the application of $M(r)$ and the finite counting statistics will generate oscillations around the density line in the measured functions. If the low- r oscillations in one of these r -space functions are set to the values given by the density line and the function is Fourier transformed to k -space, this back Fourier transform should be in agreement with the measured dataset at all k -values.²¹ The level of agreement between a measured dataset and the back Fourier transform therefore gives a measure of the accuracy of the diffraction results. In the initial analysis of the datasets using the published value for the scattering length of ²⁵Mg,¹⁸ this self-consistency check was not obeyed, which pointed to the need for a remeasurement of the scattering length for this isotope.

To accommodate the effect of the window function, each peak i in $rg_{\alpha\beta}(r)$ was represented by the Gaussian function

$$p_{\alpha\beta}^i(r) = \frac{1}{4\pi\rho} \frac{\tilde{n}_{\alpha}^{\beta}(i)}{c_{\beta}^i r_{\alpha\beta}^i} \frac{1}{\sqrt{2\pi\sigma_{\alpha\beta}^i}} \exp\left[-\frac{(r - r_{\alpha\beta}^i)^2}{2(\sigma_{\alpha\beta}^i)^2}\right], \quad (13)$$

where $r_{\alpha\beta}^i$, $\sigma_{\alpha\beta}^i$, and $\tilde{n}_{\alpha}^{\beta}(i)$ are the peak position, standard deviation, and coordination number of chemical species β around α , respectively. In the neutron diffraction work, a measured r -space function was fitted to a suitable sum of these Gaussian peaks, convoluted with $M(r)$, using the procedure described in Ref. 22. The goodness-of-fit was assessed by the parameter R_{χ} .²³

In the x-ray diffraction work, the total pair-distribution function $D'_{\text{X}}(r)$ was obtained from Eq. (6) after replacing $F_{\text{N}}(k) / \langle b \rangle^2$ by $S_{\text{X}}(k) - 1 = F_{\text{X}}(k) / \langle f(k) \rangle^2$. The contribution of each Gaussian peak $p_{\alpha\beta}^i(r)$ to $S_{\text{X}}(k) - 1$ was calculated and then Fourier transformed to real space using the same $M(k)$ function as used for the experimental data.²² A least squares procedure was used to fit an appropriate sum of these Fourier transforms to the function $T'_{\text{X}}(r) = T_{\text{X}}(r) \otimes M(r)$ using the program PXFIT,⁸⁰ where

$T_X(r) \equiv D_X(r) + T_X^0(r)$ and $T_X^0(r) = 4\pi r$. The fitted functions are presented as $D_X(r) = [T_X(r) - T_X^0(r)] \otimes M(r) = T_X'(r) - 4\pi r$ for ease of comparison with the neutron diffraction results. The goodness-of-fit was also assessed by the parameter R_X^{23} as calculated for the $D_X'(r)$ representation of the x-ray datasets.

III. EXPERIMENT

A. Sample preparation and characterization

The enstatite samples were prepared using the method described in Ref. 16 from either ^{nat}MgO (>99%) or isotopically enriched ^{25}MgO and SiO_2 (>99%). The isotopic enrichment of ^{25}Mg was measured to be 1.00(2)% ^{24}Mg , 98.49(3)% ^{25}Mg , and 0.51(1)% ^{26}Mg using Inductively Coupled Plasma Mass Spectrometry (ICP-MS).

The isotopically enriched diopside glass was made from powders of ^{25}MgO (0.81% ^{24}Mg , 98.79% ^{25}Mg , 0.40% ^{26}Mg), CaCO_3 (>99%), and SiO_2 (>99%) using the method described in Ref. 24. The powders were calcined overnight at 800 °C and were then melted in air at a processing temperature $T_{\text{proc}} \sim 1492$ °C in a Pt/10%Rh crucible. The melt was quenched by immersing the bottom of the crucible in water. The melt and quench process was repeated to ensure a homogeneous glass. The diopside glass of natural isotopic abundance was prepared from powders of ^{nat}MgO (Aldrich, $\geq 99.99\%$), CaCO_3 (Aldrich, $\geq 99.999\%$), and SiO_2 (Alfa Aesar, 99.9%). The powders were calcined overnight at 800 °C and mixed by shaking. A batch of mass ~ 3 g was transferred to a Pt/10%Rh crucible, melted by heating from room temperature to $T_{\text{proc}} = 1550$ °C in about 1 h, and held at this temperature for 1 h. The melt was quenched by placing the bottom of the crucible onto a liquid-nitrogen cooled copper block. The sample was then ground, remelted in a furnace at 1550 °C for 1 h, and quenched again. The mass loss was 0.08% on the first melt and 0.15% on the second melt, which was attributed to the loss of water re-adsorbed during the preparation procedure.

The aluminosilicate samples are designated by $\text{MgAS}_x\text{-(}100\text{-}x\text{-}y\text{)}$ with x and y expressed in mol. %. They were prepared from either ^{nat}MgO (Aldrich, $\geq 99.99\%$) or isotopically enriched ^{25}MgO (Isoflex, 0.32% ^{24}Mg , 99.38% ^{25}Mg , 0.30% ^{26}Mg), Al_2O_3 (Sigma-Aldrich, 99.998%), and SiO_2 (Alfa Aesar, 99.9%). The powders were calcined at 1000 °C for 2 h in a Pt or Pt/10%Rh crucible.

For the $\text{MgAS}_{37.5_50}$ and MgAS_{25_50} samples, an appropriate mass of each powder was mixed by shaking. The mixture was then transferred to a Pt/10%Rh crucible and dried at 1000 °C for 10 min to remove water adsorbed during the weighing and mixing process. Each batch of mass ~ 3 g was melted by heating from room temperature to a temperature T_{proc} of either 1550 °C ($\text{MgAS}_{37.5_50}$) or 1650 °C (MgAS_{25_50}) in about 1 or 1.25 h, respectively, and was then held at this temperature for 1 h. The melt was quenched by placing the bottom of the crucible onto a liquid-nitrogen cooled copper block. The mass loss on melting was <0.3%, which was attributed to the loss of re-adsorbed water.

The MgAS_{30_60} and MgAS_{20_60} glasses were made by adding SiO_2 to either $\text{MgAS}_{37.5_50}$ or MgAS_{25_50} , respectively, after the latter had been finely ground and dried at 200 °C for 1 h. The powders were mixed by shaking. Each batch of mass ~ 2 g was melted in a Pt/10%Rh crucible by putting that crucible into a furnace at 1650 °C for 1 h. The melt was quenched by placing the bottom of the crucible onto a liquid-nitrogen cooled copper block.

TABLE I. The processing temperature T_{proc} and number density ρ of the diopside, enstatite, and MgAS glasses.

Sample	x	y	T_{proc} (°C)	ρ (\AA^{-3})
Diopside	1492–1550	0.0786(1)
Enstatite	0.4939	0	1650	0.0806(1)
$\text{MgAS}_{37.5_50}$	0.375	0.125	1550	0.0804(1)
MgAS_{25_50}	0.250	0.250	1650	0.0795(1)
MgAS_{30_60}	0.300	0.100	1650	0.0771(1)
MgAS_{20_60}	0.200	0.200	1650	0.0766(1)

Each sample was ground before the melting and quench process was repeated. The mass loss was $\leq 0.46\%$ on the first melt and $\leq 0.29\%$ on the second melt, which was attributed to the loss of re-adsorbed water.

The stoichiometry of the enstatite glasses was measured using electron microprobe analysis and the density was measured using Archimedes's principle with toluene as the immersion medium.¹⁶ The stoichiometry of the other glasses was taken from the batch composition and their density was measured by He pycnometry (Table I).

For each glass composition, the electronic structure will not depend on isotope enrichment, so the x-ray diffraction patterns measured for the ^{nat}Mg and ^{25}Mg samples should be the same within statistical error. Figure 1 shows this is the case to a good level of approximation for the investigated MgAS materials. The agreement for the diopside glass is less satisfactory, which likely originates from differences in the sample preparation procedure for the ^{nat}Mg and ^{25}Mg samples.

Crystalline samples of ^{nat}MgO and ^{25}MgO , of mass 195.6 and 312.3 mg, respectively, were prepared from the enstatite glasses. The silicate was placed in a polytetrafluoroethylene (PTFE) beaker and dissolved in 40% hydrofluoric acid. The resulting solution was evaporated, several milliliters of concentrated sulfuric acid were then added, and the solution was re-evaporated. The resulting MgSO_4 was transferred to a corundum crucible and fired at 1200 °C for 3 h to obtain pure MgO. The isotopic abundance of ^{nat}Mg was measured to be 74.6(2)% ^{24}Mg , 11.0(1)% ^{25}Mg , and 14.4(1)% ^{26}Mg using ICP-MS. In comparison, the standard isotopic abundance of ^{nat}Mg , as used in the preparation of standard tables of neutron scattering lengths,^{25,26} is 78.992(25)% ^{24}Mg , 10.003(9)% ^{25}Mg , and 11.005(19)% ^{26}Mg .²⁷

B. Neutron powder diffraction

The instrument D4c at the Institut Laue-Langevin²⁸ was used to perform diffraction experiments on the powdered crystalline samples because of the high flux of incident neutrons and its ability to deliver diffraction patterns with excellent reproducibility and count-rate stability.²⁹ The incident neutron wavelength λ was either 0.4971(5) or 0.6983(4) Å, as found from a Rietveld refinement of the diffraction pattern measured for a powdered nickel standard, and the $\lambda/2$ scattering from the monochromator was removed using either a Rh or Ir filter, respectively. In each experiment, powder diffraction patterns were measured for the ^{25}MgO or ^{nat}MgO sample in a cylindrical vanadium container of inner diameter 4.78 mm and wall thickness 0.3 mm, the empty container, the empty instrument,

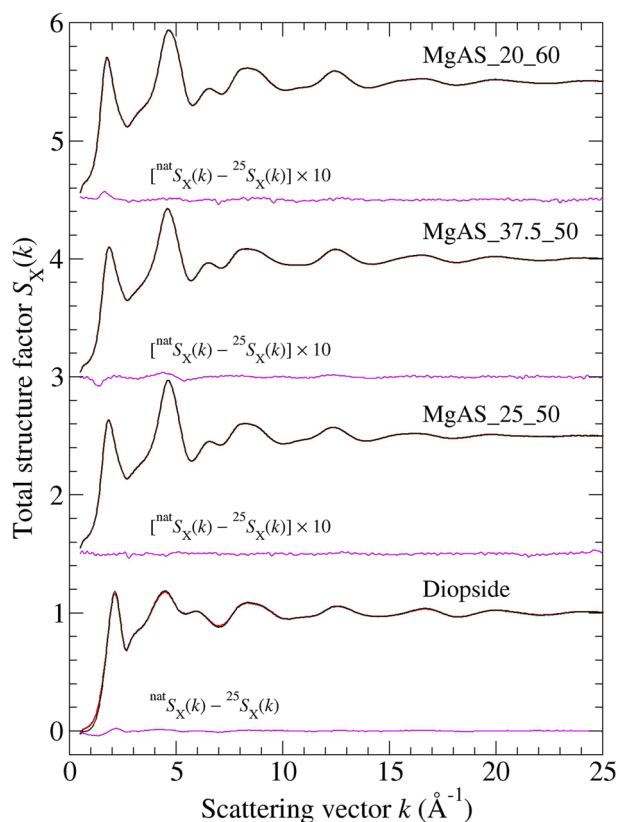


FIG. 1. The $S_X(k)$ functions measured for diopside glass and for several of the MgAS glasses containing either ^{nat}Mg (black curves) or ^{25}Mg (red curves). For each of the MgAS glasses, the curves overlay on the scale of the plot, as emphasized by taking the difference between them and multiplying by a factor of ten (magenta curves). Several of the curves are displaced vertically for clarity of presentation.

and a cylindrical vanadium rod of diameter 6.08 mm for normalization purposes. In these experiments, the longer wavelength leads to improved resolution of the Bragg peaks in a powder diffraction pattern at the expense of a reduction in k_{max} .

For each wavelength, the datasets were processed in two different ways. In the first procedure, the diffraction pattern for the sample in its container was corrected for background and container scattering by subtracting a linear combination of the diffraction patterns for the empty instrument and empty container. Corrections for sample attenuation and multiple scattering were then applied. In the second procedure, the total structure factor $F_N(k)$ was obtained using the procedure described in Ref. 21, which takes into account sample and container attenuation, multiple scattering from both the sample and container, and inelasticity corrections. Finally, the variable was changed from k to the scattering angle 2θ by using the expression $k = (4\pi/\lambda) \sin(\theta)$.¹⁷

A Rietveld refinement was performed on each dataset, represented as a function of 2θ , using both the FullProf (version 7.60)^{30,31} and GSAS-II (version 5241)³² packages. In each refinement, the scattering length $b_{\text{O}} = 5.805(4)$ fm^{25,33} and a rock-salt structural

model was employed. The zero-point shift and overall scale factor were initially refined, followed by the cell parameter a and thermal displacement parameters for the Mg and O atoms. The background originating from diffuse scattering was fitted using a twelfth-order Chebyshev polynomial. In FullProf, the peak shapes were fitted using the pseudo-Voigt function $pV(x) = \tilde{\eta}L(x) + (1 - \tilde{\eta})G(x)$, which has both Lorentzian $L(x)$ and Gaussian $G(x)$ contributions, with the variable $x = \theta - \theta_h$, where θ_h is the Bragg peak position and $\tilde{\eta}$ ($0 \leq \tilde{\eta} \leq 1$) is a weighting factor. The full-width at half-maximum (FWHM) of the Gaussian function is given by the Caglioti relation $\text{FWHM}^2 = U \tan^2 \theta + V \tan \theta + W$.^{34,35} The parameters U , V , W , and $\tilde{\eta}$ were obtained by refinement along with two asymmetry parameters.³¹ In GSAS, the peak shapes were fitted using an axial-divergence-broadened pseudo-Voigt function with the FWHM of the Gaussian function given by the Caglioti relation. The parameters U , V , W , and $\tilde{\eta}$ were refined along with the axial-divergence asymmetry parameter SH/L .

In a Rietveld refinement, the scattering length of magnesium cannot be obtained directly (Sec. II A). Instead, it was found by refining the occupation factor for the Mg atom after the magnesium scattering length is set to the published value of $b_{^{25}\text{Mg}} = 3.62(14)$ fm¹⁸ for the ^{25}MgO sample or $b_{^{nat}\text{Mg}} = 5.375(4)$ fm³⁶ for the ^{nat}MgO sample. The set magnesium scattering length is then multiplied by the refined occupation factor to give a corrected value, which is denoted by $\tilde{b}_{^{25}\text{Mg}}$ or $\tilde{b}_{^{nat}\text{Mg}}$, respectively, and corresponds to the isotopic enrichment of magnesium in the measured sample.

In total, for each of the ^{25}MgO and ^{nat}MgO samples, eight values of the magnesium scattering length were generated. The values did not show any obvious dependence on (i) the λ value chosen for the diffraction experiment, (ii) the procedure used to process the diffraction patterns, or (iii) the software package used for the Rietveld refinement. The mean value of the scattering length for a given sample was therefore calculated using all the available results and the error was found from the standard deviation about the mean.

C. ^{29}Si and ^{27}Al MAS NMR

The ^{29}Si magic angle spinning (MAS) NMR spectra were recorded at room temperature at a magnetic flux density of 5.64 or 14.1 T using an Agilent DD2 or Bruker Avance Neo 600 spectrometer, respectively, equipped with commercial MAS NMR probes. The investigated samples were isotopically enriched with ^{25}Mg . The spectra for the diopside and enstatite glasses were measured at 5.64 T using 4.0 mm rotors spun at 5 kHz, 90° pulses of $4 \mu\text{s}$ length, and a relaxation delay of 900 s.⁸ The spectra for the MgAS glasses were measured at 14.1 T using 2.5 mm rotors spun at 10 kHz, 90° pulses of $2.7 \mu\text{s}$ length, and a relaxation delay of 900 s.

The ^{27}Al MAS NMR spectra were recorded at room temperature at a magnetic flux density of 14.1 T on the Bruker Avance Neo 600 spectrometer, using 2.5 mm rotors, spinning rates between 15 and 25 kHz, 90° pulses of $1.2 \mu\text{s}$ length, and a relaxation delay of 0.5 s. The samples were isotopically enriched with ^{25}Mg or contained magnesium of natural isotopic abundance. The ^{27}Al triple-quantum magic angle spinning (TQMAs) experiments³⁷ utilized the standard three-pulse zero-filtering sequence, with pulse lengths of 3.9 and $1.7 \mu\text{s}$ for the creation and conversion of triple-quantum coherences, respectively, with a power level of 120 W. The soft detection pulse

applied for the zero-to-single quantum conversion had a length of 10.2 μs with a power level of 1.5 W. The relaxation delay was 0.1 s. A series of free induction decay (FID) signals in the TQMAS measurements was Fourier transformed and sheared using the software TopSpin to obtain the separate isotropic (F1) and anisotropic (F2) dimensions. The isotropic chemical shift δ_{iso} and quadrupolar product P_{Q} were derived from the sheared two-dimensional spectra using the expressions³⁸

$$\delta_{\text{iso}} = \frac{17}{27}\delta_1 + \frac{10}{27}\delta_2 \quad (14)$$

and

$$P_{\text{Q}} = C_{\text{Q}} \left(1 + \frac{\eta^2}{3}\right)^{\frac{1}{2}} \\ = \sqrt{\left\{ \frac{170}{81} \frac{[4S(2S-1)]^2}{[4S(S+1)-3]} (\delta_1 - \delta_2) \right\}} \times \nu_0 \times 10^{-3}. \quad (15)$$

Here, δ_1 and δ_2 are the chemical shifts in the F1 and F2 dimensions obtained from integration over the regions of interest, respectively, C_{Q} and η ($0 \leq \eta \leq 1$) are parameters that describe the magnitude and symmetry of the electric field gradient tensor interacting with the nuclear electric quadrupole moment, respectively, ν_0 is the Zeeman frequency, and S is the spin quantum number of the nucleus.

The MAS NMR spectra were simulated using the DMfit program.³⁹ Gaussian/Lorentzian line shapes were assumed for (i) the spin-1/2 ^{29}Si nucleus and (ii) the spinning sidebands associated with the $|m| = 1/2 \leftrightarrow |m| = 3/2$ satellite transitions for the ^{27}Al nucleus (for spin-5/2 nuclei, the second-order quadrupolar broadening effects are negligible for these transitions⁴⁰). In the above, m represents the magnetic quantum number. The ^{27}Al central-transition line shapes were simulated with the Czjzek model,⁴¹ which is based on the assumption of a wide distribution of quadrupolar coupling strengths.

The ^{29}Si and ^{27}Al chemical shifts are reported relative to tetramethylsilane (TMS) and 1M $\text{Al}(\text{NO}_3)_3$ aqueous solution, respectively, using solid kaolinite [$\delta_{\text{iso}}(^{29}\text{Si}) = -91.5$ ppm] and AlF_3 [$\delta_{\text{iso}}(^{27}\text{Al}) = -16$ ppm] as secondary references, respectively.

D. ^{25}Mg MAS and static NMR

The ^{25}Mg MAS NMR spectra were measured at room temperature at a magnetic flux density of 14.1 T (36.8 MHz) in the form of rotor-synchronized Hahn spin echoes on the Bruker Avance Neo 600 spectrometer using 3.2 mm rotors spun at 20.0 kHz. Experiments were performed at two different power levels corresponding to nonselective nutation frequencies ν_1 of 25 and 80 kHz (measured on cubic MgO). The effective 90° pulse lengths were optimized by maximizing the echo intensity in a $t_p - \tau - 2t_p - \tau$ acquisition scheme, with $\tau = 50$ μs and t_p values of 9 and 3.5 μs , respectively, for the two nutation frequencies employed. The relaxation delay was 0.5 s.

The static ^{25}Mg NMR spectra were measured using a Wide-band Uniform Rate Smooth Truncation (WURST) pulse sequence⁴² combined with the Carr–Purcell–Meiboom–Gill (CPMG) echo train acquisition scheme.^{43,44} To cover a wide-frequency range, the signal

was acquired at multiple distinct base frequencies, corresponding to resonance offsets from the center of the $m = 1/2 \leftrightarrow m = -1/2$ transition of ± 5000 , $\pm 10\,000$ ppm and up to $\pm 30\,000$ ppm. These spectra were recorded with the objective of testing for the presence of non-central ($|m| = 1/2 \leftrightarrow |m| = 3/2$ and $|m| = 3/2 \leftrightarrow |m| = 5/2$) satellite transitions, which are affected to different extents by the anisotropy of nuclear electric quadrupolar interactions. The WURST experiments were performed using excitation and refocusing pulses with an identical length of 50.0 μs , an excitation bandwidth of 1 MHz, and a recycle delay of 0.2 s. The pulse spacing was set to give a spikelet separation of 6.7 kHz upon Fourier transformation and the number of Meiboom–Gill loops was set to 256.

The simulations of the ^{25}Mg MAS line shape used the Czjzek model and were performed using the ssNake⁴⁵ software. The simulations of the ^{25}Mg static line shapes also used the Czjzek model and were performed using in-house Matlab[®] code with SIMPSON⁴⁶ as the kernel. Details of the simulation procedures are described elsewhere.⁸

The ^{25}Mg chemical shifts are reported relative to aqueous MgCl_2 solution using solid $^{\text{nat}}\text{MgO}$ [$\delta_{\text{iso}}(^{25}\text{Mg}) = 27$ ppm] as a secondary reference.

E. Neutron diffraction with isotope substitution

The neutron diffraction with isotope substitution work on the amorphous materials employed the diffractometer D4c,²⁸ chosen because of the attributes described in Sec. III B and its ability to access a wide k -range.

The incident neutron wavelength was $\lambda = 0.4958(1)$ \AA for the experiments on the diopside, MgAS_{25_50} and $\text{MgAS}_{37.5_50}$ compositions, $\lambda = 0.4955(1)$ \AA for the experiment on the MgAS_{20_60} composition, and $\lambda = 0.4978(1)$ \AA for the experiment on the MgAS_{30_60} composition. In each experiment, the coarsely ground samples were held in a cylindrical vanadium container of inner diameter 4.8 mm (diopside or MgAS_{30_60}) or 6.8 mm (all other samples) and wall thickness 0.1 mm. The same container was used for both samples of a given glass composition in order to reduce the occurrence of systematic errors.²¹ Diffraction patterns were measured at room temperature (≈ 298 K) for each of the samples in its container, the empty container, the empty instrument, and a cylindrical vanadium rod of diameter 6.08 mm for normalization purposes. The relative counting times for the sample-in-container and empty container measurements were optimized in order to minimize the statistical error on the container corrected intensity.⁴⁷ Data analysis followed the procedure described in Ref. 21.

The diffraction experiments on the enstatite glasses also used D4c with $\lambda = 0.497$ \AA .¹⁶ The raw datasets were reanalyzed using the new scattering length for ^{25}Mg (Sec. IV A) following the same procedure used for the other glass samples.²¹

F. X-ray diffraction

The x-ray diffraction experiments were performed at room temperature using beamline 6-ID-D at the Advanced Photon Source with an incident photon energy of 100.233 keV. A Varex 4343CT amorphous silicon flat panel detector was employed with the sample to detector distance set at 311 mm as found from the diffraction pattern measured for crystalline CeO_2 . Powdered glass samples were held in cylindrical Kapton polyimide tubes of 1.80(1) mm internal diameter and 0.051(6) mm wall thickness. Diffraction patterns were

measured for each sample in its container, an empty container, and the empty instrument. The data were converted to one-dimensional diffraction patterns using FIT2D.⁴⁸ The background scattering, beam polarization, attenuation and Compton scattering corrections were performed using PDFgetX2.⁴⁹

IV. RESULTS

A. ²⁵Mg neutron scattering length

Figure 2 shows the powder diffraction patterns for the crystalline ²⁵MgO and ^{nat}MgO samples measured at both neutron wavelengths, where the raw datasets were processed by using the first correction procedure described in Sec. III B. The diffraction patterns were refined using both the FullProf (see Fig. 2) and GSAS-II packages. As a consistency check, the raw datasets were also processed using the second correction procedure described in Sec. III B, and the corrected diffraction patterns were refined using

both Rietveld refinement packages. For a given sample, the results from all these measurements were the same, within the experimental error.

Both the ²⁵MgO and ^{nat}MgO samples contain finite amounts of all three of the stable magnesium isotopes ²⁴Mg, ²⁵Mg, and ²⁶Mg. The system of linear equations for extracting all three of the scattering length values is therefore under-determined, so we adopted an iterative approach to obtain a consistent set of values.

For the ²⁵MgO sample, an average value $\tilde{b}_{25\text{Mg}} = 3.745(10)$ fm was obtained from the Rietveld refinements of all the diffraction patterns, where the tilde indicates a contribution from small amounts of the ²⁴Mg and ²⁶Mg isotopes. To correct for this contribution, the scattering lengths $b_{24\text{Mg}} = 5.66(3)$ fm²⁶ and $b_{26\text{Mg}} = 4.89(15)$ fm¹⁸ were initially employed, along with the isotopic abundance of our ²⁵Mg sample as measured by ICP-MS (Sec. III A). Here, the reported value for $b_{24\text{Mg}}$ was calculated from the value $b_{\text{natMg}} = 5.375(4)$ fm measured by neutron interferometry³⁶ using the values $b_{25\text{Mg}} = 3.62(14)$ fm and $b_{26\text{Mg}} = 4.89(15)$ fm found in

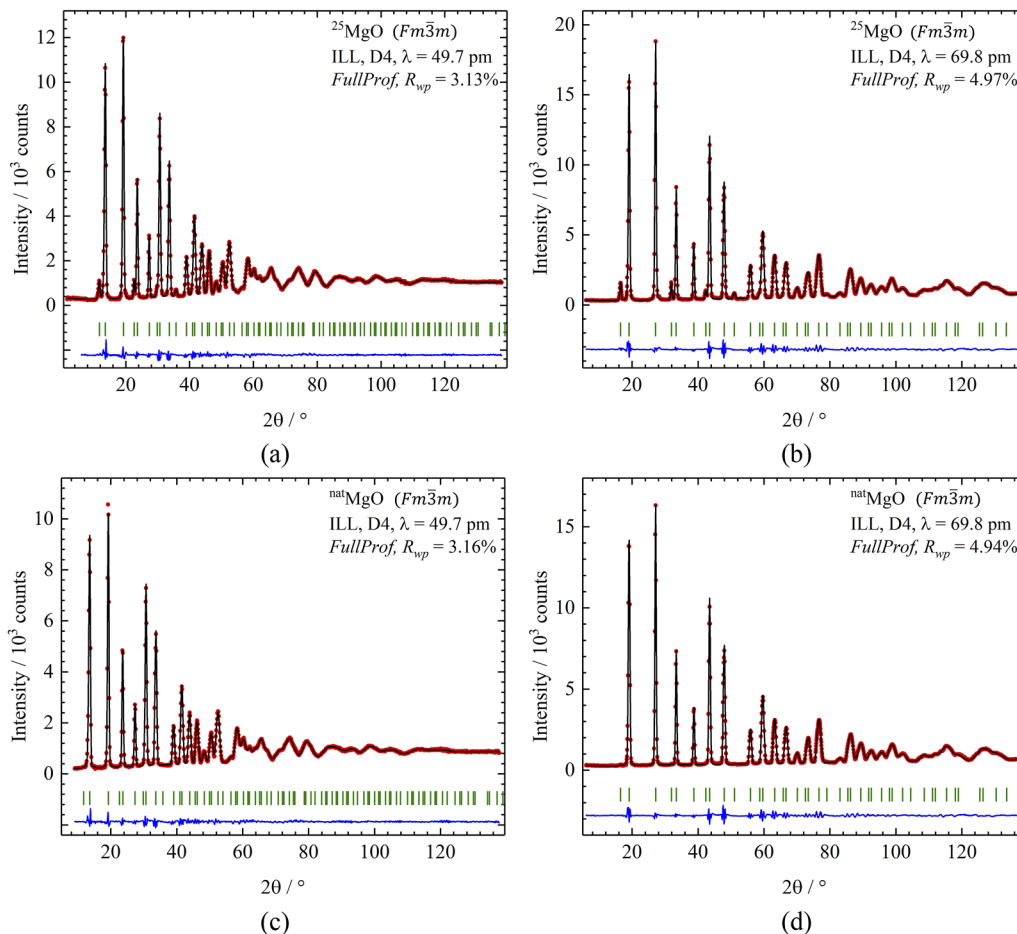


FIG. 2. Powder diffraction patterns measured for (a) and (b) ²⁵MgO vs (c) and (d) ^{nat}MgO crystalline samples at different incident neutron wavelengths and the Rietveld refinements using FullProf. Each panel shows the measured intensity I_{obs} (red circles), calculated intensity I_{calc} (black curve), and the difference of intensities $I_{\text{obs}} - I_{\text{calc}}$ (blue curve), along with the positions of Bragg reflections allowed by the space group for the structure (vertical green bars). R_{wp} denotes the weighted profile R -factor.

TABLE II. Bound coherent neutron scattering lengths for $^{\text{nat}}\text{Mg}$ and the isotopes of magnesium.

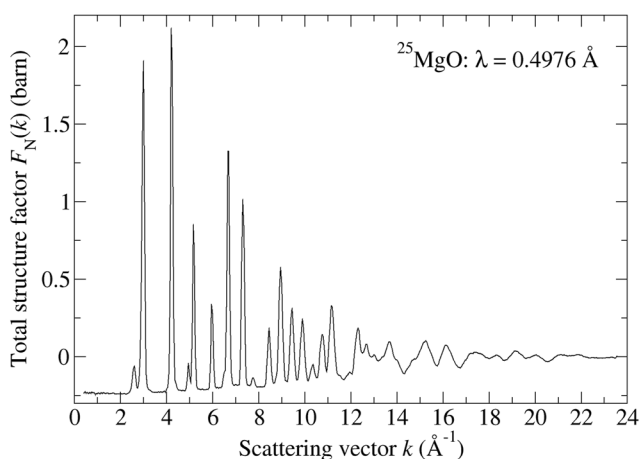
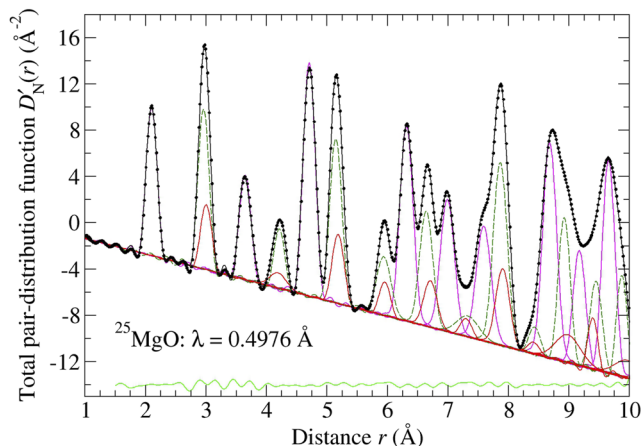
Species	b (fm)	Reference
$^{\text{nat}}\text{Mg}$	5.375(4)	36
^{24}Mg	5.65(3)	This work
^{25}Mg	3.720(12)	This work
^{26}Mg	4.89(15)	18

previous neutron powder diffraction work¹⁸ and the standard isotopic abundance of $^{\text{nat}}\text{Mg}$ reported in Ref. 27, where $b_{24\text{Mg}}$ is the dominant isotope (Sec. III A). Hence, a new value for $b_{25\text{Mg}}$ was obtained, leading to a new value for $b_{24\text{Mg}}$ and, in turn, a new value for $b_{25\text{Mg}}$. This iterative procedure converged rapidly and the high isotopic enrichment of the ^{25}MgO sample led to a small correction of the order 0.7%. The final scattering length values are listed in Table II.

For the $^{\text{nat}}\text{MgO}$ sample, an average value $\tilde{b}_{\text{natMg}} = 5.304(35)$ fm was obtained from the Rietveld refinements of all the diffraction patterns, where the tilde indicates the isotopic abundance of our $^{\text{nat}}\text{Mg}$ sample as measured by ICP-MS (Sec. III A). In comparison, the value $\tilde{b}_{\text{natMg}} = 5.328(31)$ fm is obtained from the scattering lengths for the magnesium isotopes listed in Table II and the isotopic abundance of our $^{\text{nat}}\text{Mg}$ sample. The discrepancy between these scattering lengths is 0.45%, which is within the precision of the measurements.

For completeness, the value $b_{\text{natMg}} = 5.373(29)$ fm is obtained from the scattering lengths for the magnesium isotopes listed in Table II and the standard isotopic abundance of $^{\text{nat}}\text{Mg}$ reported in Ref. 27 (Sec. III A), which is in agreement with the value $b_{\text{natMg}} = 5.375(4)$ fm measured using neutron interferometry.³⁶ The scattering lengths listed in Table II are therefore self-consistent, although the values for ^{24}Mg and ^{26}Mg should be remeasured.

Finally, the $F_N(k)$ function measured for the ^{25}MgO sample using $\lambda = 0.4976$ Å, and corrected using the measured value

**FIG. 3.** The $F_N(k)$ function for crystalline ^{25}MgO measured using $\lambda = 0.4976$ Å. The measured function is shown by the black curve with vertical error bars, where the error bars are smaller than the curve thickness at most k -values.**FIG. 4.** The $D'_N(r)$ function for crystalline ^{25}MgO . The measured function (black solid circles) was obtained by Fourier transforming the $F_N(k)$ function shown in Fig. 3 with $k_{\text{max}} = 23.55$ Å⁻¹ and $\rho = 0.1070$ Å⁻³. The black solid curve gives the fitted function and the other curves show the contributions from the Mg–O (magenta solid curves), O–O (green broken curves), and Mg–Mg (red solid curves) correlations. The displaced green solid curve shows the residual for the fitted range 1.5–10.0 Å ($R_\chi = 0.0295$).

$\tilde{b}_{25\text{Mg}} = 3.745(10)$ fm that takes into account the isotopic enrichment, is shown in Fig. 3. Here, the wavelength was found from the diffraction pattern measured for the powdered nickel standard by fitting the five Bragg peaks that occur in the range $12^\circ \leq 2\theta \leq 30^\circ$ using a procedure in which the wavelength and zero-angle 2θ offset are varied, keeping the lattice parameter determining the Bragg peak positions fixed and allowing the parameters describing the intensity and shape of the Lorentzian–Gaussian peak profiles to vary. The 0.1% discrepancy with the value found from the Rietveld refinement of the same nickel diffraction data is well within the precision of the measurements. For comparison with the glass structures, the corresponding $D'_N(r)$ function is shown in Fig. 4 and was fitted by constraining the coordination numbers of the fitted Gaussian peaks to the values expected for the measured crystal structure.² The first peak in $D'_N(r)$ originates from Mg–O correlations and is symmetrical, corresponding to a bond distance of 2.102(2) Å and coordination number $\tilde{n}_{\text{Mg}}^{\text{O}} = 6.00$.

B. Solid-state NMR

1. ^{29}Si MAS NMR

Figure 5 shows the ^{29}Si MAS NMR spectra for the isotopically enriched samples. The signal-to-noise ratio is low because of the small sample size. The resonances are poorly resolved and, for the MgAS glasses, no sensible peak deconvolution was possible. Such poor resolution is expected from the large variety of possible silicon local coordination environments generated by the interaction of silicon with both the network modifier and aluminum species. The resonance positions are consistent with four-coordinated Si atoms.⁵¹

In alumina free glasses, the introduction of a network modifier oxide to silica leads to the breakage of Si–O–Si linkages and

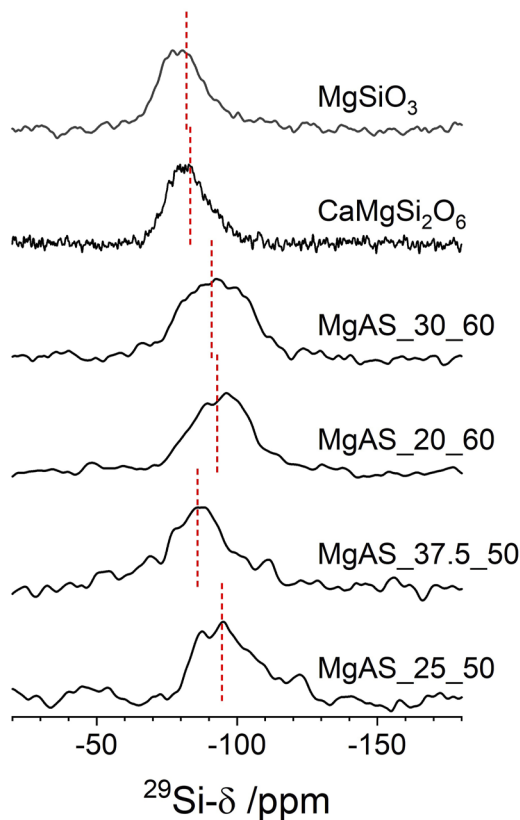


FIG. 5. The ^{29}Si MAS NMR spectra measured for ^{25}Mg enriched magnesium silicate and aluminosilicate glasses. The datasets for enstatite and diopside are from Ref. 8. The red broken vertical lines mark the center of gravity of each peak shape.

the formation of non-bridging oxygen (NBO) atoms. The tetrahedral $[\text{SiO}_{4/2}]^0$ units of pure silica glass, where O denotes a bridging oxygen (BO) atom, are thereby converted to tetrahedral $[\text{SiO}_{3/2}\text{O}]^-$, $[\text{SiO}_{2/2}\text{O}_2]^{2-}$, $[\text{SiO}_{1/2}\text{O}_3]^{3-}$, and $[\text{SiO}_4]^{4-}$ units. These silicon species are designated by Q^n , where n is the number of Si-BO bonds within a tetrahedron, and can be identified and quantified from a deconvolution of the measured ^{29}Si MAS NMR spectra.⁵¹ The results for the diopside and enstatite glasses are reported in Ref. 8.

The spectra for vitreous aluminosilicates are, however, more complicated.^{52,53} In the standard model for $(\text{MO})_x(\text{Al}_2\text{O}_3)_y(\text{SiO}_2)_{1-x-y}$ glasses containing divalent modifier cations M^{2+} with $R = x/y \geq 1$, which comprises the glass compositions relevant to this study, all the aluminum is present in the form of $[\text{AlO}_{4/2}]^-$ units. These units can form Si-O-Al linkages and their formal negative charge is compensated by the positive charge associated with M^{2+} ions. The M^{2+} species that fulfill this role are referred to as charge-compensating cations. All the NBO atoms are associated with the silicon atoms such that the probability of an Si-NBO bond is given by $p_{\text{Si-NBO}} = N_{\text{NBO}}/4N_{\text{Si}}$, where N_{NBO} and N_{Si} are the numbers of NBO and Si atoms, respectively.

Both the ligation of Si to NBO atoms and its ligation to $[\text{AlO}_{4/2}]^-$ units are expected to shift the ^{29}Si resonance toward higher (less negative) frequencies.⁵⁴ Along a tie-line with fixed

mol. % silica in the regime where $R \geq 1$, the NBO to silicon atom ratio $N_{\text{NBO}}/N_{\text{Si}}$ will decrease as MO is replaced by Al_2O_3 , thus shifting the ^{29}Si resonance toward lower (more negative) frequencies. In contrast, as the mole fraction of alumina increases there is a greater propensity for Si-O-Al linkages, thus shifting the ^{29}Si resonance in the opposite direction, i.e., toward higher (less negative) frequencies. In consequence, there are two competing effects on the shift in position of the ^{29}Si resonance.

The composition dependence of $N_{\text{NBO}}/N_{\text{Si}}$ can be calculated from the glass composition.⁵⁰ The number of Si-O-Al linkages per silicon atom $N_{\text{Si-O-Al}}/N_{\text{Si}}$ can be estimated by first assuming a binomial distribution of Si-BO and Si-NBO bonds such that the fraction of Q^n species is given by

$$f_{Q^n} = \frac{4!}{n!(4-n)!} (1 - p_{\text{Si-NBO}})^n p_{\text{Si-NBO}}^{(4-n)}. \quad (16)$$

A binomial distribution of Si-O-Si and Si-O-Al linkages, in which the probability of an Si-O-Al linkage is given by $p_{\text{Si-O-Al}} = N_{\text{Al}}/(N_{\text{Si}} + N_{\text{Al}})$ where N_{Al} is the number of Al atoms,⁵⁵ can then be used to find the fraction of Q^n species that form m Si-O-Al bonds ($m \leq n$). These species are denoted by $Q_{m\text{Al}}^n$ and their fraction is given by

$$f_{Q_{m\text{Al}}^n} = \frac{n!}{m!(n-m)!} p_{\text{Si-O-Al}}^m (1 - p_{\text{Si-O-Al}})^{(n-m)}. \quad (17)$$

In this way, the overall fraction of the Si-centered tetrahedral units that form $Q_{m\text{Al}}^n$ species can be deduced and the ratio $N_{\text{Si-O-Al}}/N_{\text{Si}}$ can be calculated.

Figure 6 compares the R dependence of the ratios $N_{\text{NBO}}/N_{\text{Si}}$, $N_{\text{Si-O-Al}}/N_{\text{Si}}$, and $N_{\text{NBO}}/N_{\text{Si-O-Al}}$ calculated for the standard model along both the 50 and 60 mol.% silica tie-lines. The ratio $N_{\text{NBO}}/N_{\text{Si}} \rightarrow 0$ as $R \rightarrow 1$ and the ratio $N_{\text{NBO}}/N_{\text{Si-O-Al}}$ varies linearly (50 mol. % silica) or almost linearly (60 mol. % silica) with R . The results confirm that the observed shift of the ^{29}Si resonance toward smaller (more negative) chemical shifts in the investigated MgAS glasses as $R \rightarrow 1$ (Table III) is associated with a decrease in the

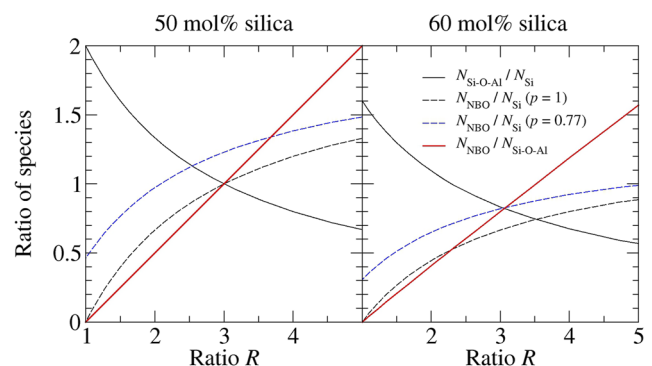


FIG. 6. The R dependence of the ratios $N_{\text{Si-O-Al}}/N_{\text{Si}}$ (black curves), $N_{\text{NBO}}/N_{\text{Si}}$ (black broken curves), and $N_{\text{NBO}}/N_{\text{Si-O-Al}}$ (red curves) for the standard model ($p = 1$) of aluminosilicate glass. The ratio $N_{\text{NBO}}/N_{\text{Si}}$ for the GYZAS model of magnesium aluminosilicates with $p = 0.77$ ⁵⁰ is also given (blue broken curves). The ratios are calculated for tie-lines with either 50 mol. % silica (left column) or 60 mol. % silica (right column).

TABLE III. Center of gravity of the ^{29}Si MAS NMR spectra measured for ^{25}Mg enriched silicate and aluminosilicate glasses. For the latter, the ratio $R = x/y$ is given. The results for diopside and enstatite are taken from Ref. 8.

Glass	$\delta_{\text{CG}} (\pm 3 \text{ ppm})$	R
Diopside	-84	...
Enstatite	-83	...
$^{25}\text{MgAS}_{37.5_50}$	-86	3
$^{25}\text{MgAS}_{25_50}$	-95	1
$^{25}\text{MgAS}_{30_60}$	-91	3
$^{25}\text{MgAS}_{20_60}$	-93	1

$N_{\text{NBO}}/N_{\text{Si-O-Al}}$ ratio. This shift is smaller for the 60 mol. % silica tie-line where, for the investigated R -range, the fractional change in $N_{\text{NBO}}/N_{\text{Si-O-Al}}$ is concomitantly smaller.

The above considerations are, nevertheless, approximate because the high cation field strength of Mg^{2+} will promote the formation of a fraction of higher-coordinated aluminum species when $R \geq 1$ ⁵⁰ and because NBO atoms associated with Al species are neglected. The influence of these changes in speciation on the ^{29}Si chemical shift is not well documented. Nevertheless, its effect on the R dependence of $N_{\text{NBO}}/N_{\text{Si}}$ can be predicted by the so-called GYZAS model of Ref. 50, in which the fraction of Al(IV) species is set by an empirical parameter p found from ^{27}Al MAS NMR experiments: $f_{\text{Al(IV)}} = (1 + p)/2$ when $R \geq 1$. As compared to the standard model, the ratio $N_{\text{NBO}}/N_{\text{Si}}$ is no longer zero at $R = 1$ (Fig. 6), i.e., the shift in the ^{29}Si resonance toward lower frequencies originating from the loss of NBO atoms will be comparatively smaller.

2. ^{27}Al MAS NMR

Figure 7 shows the central transition in the measured ^{27}Al MAS NMR spectra and the line shape fits based on the parameters listed in Table IV. The asymmetrical shape of each spectrum is characteristic of a wide distribution of quadrupolar coupling parameters. Most of the datasets could be fitted by assuming two distinct aluminum sites, with Czjzek line shape components having isotropic chemical shifts near 63 and 38 ppm. According to these chemical shifts, the first site is assigned to four-coordinated aluminum and the second site suggests the formation of five-coordinated aluminum.^{52,53} For the $^{25}\text{MgAS}_{25_50}$ sample, there is also evidence for a small fraction of six-coordinated aluminum.

To confirm the presence of five-coordinated aluminum, Fig. 8 shows representative SATellite TRansition Spectra (SATRAS) for the isotopically enriched samples. As previously discussed,⁵⁷ the allowed $m = \pm 1/2 \leftrightarrow m = \pm 3/2$ Zeeman transitions of $I = 5/2$ nuclei are broadened by the anisotropy of the nuclear electric quadrupolar interactions. However, second-order effects on these Zeeman transitions are rather weak, such that magic angle spinning transforms the inhomogeneously broadened line shape into a manifold of sharp spinning sidebands separated from each other by multiples of the spinning frequency. Thus, owing to the absence of second-order quadrupolar broadening effects, the spectroscopic resolution for these satellite-MAS-peak patterns is superior to the resolution for the central-transition line shape, as observed in Fig. 8.

The ^{27}Al MAS NMR results therefore support the presence of five-coordinated Al species in all the MgAS glasses of the present

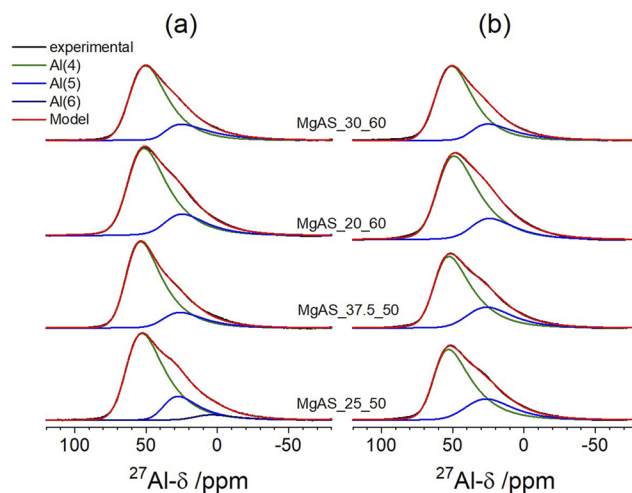


FIG. 7. The central transition in the ^{27}Al MAS NMR spectra measured for the aluminosilicate glasses containing either (a) isotopically enriched ^{25}Mg or (b) magnesium with its natural isotopic abundance. The spectra were deconvoluted using the Czjzek model.

study, with a contribution to the area of a spectrum that varies between 16% and 25%. The results for the MgAS_{20_60} glass are in good agreement with those previously obtained.^{50,58} The average coordination number $\bar{n}_{\text{Al}}^{\text{O}}$ can be deduced from the fractional areas found from the fitted spectra and are listed in Table IV. This information was used in fitting the neutron and x-ray diffraction data (Sec. IV C).

Figure 9 shows the complementary spectra measured by ^{27}Al TQMAS NMR. They confirm the presence of both four- and five-coordinated Al, and the application of Eqs. (14) and (15) yields the average isotropic chemical shifts $\langle \delta_{\text{iso}} \rangle$ and second-order quadrupolar effects $\langle P_{\text{Q}} \rangle$ listed in Table IV. For four-coordinated Al, the $\langle \delta_{\text{iso}} \rangle$ and $\langle P_{\text{Q}} \rangle$ values obtained from TQMAS NMR are in reasonable agreement. The $\langle P_{\text{Q}} \rangle$ values extracted from TQMAS NMR tend to be smaller than the $\langle |C_{\text{Q}}| \rangle$ values extracted from the MAS-Czjzek fits because of the lower triple-quantum excitation efficiency observed for the Al species at the upper end of the quadrupole coupling constant distribution. For this reason, the $\langle |C_{\text{Q}}| \rangle$ values from the MAS-Czjzek fits are considered more representative. For five-coordinated Al, the $\langle P_{\text{Q}} \rangle$ values are considerably underestimated because of the low signal-to-noise ratio. For the isotopically enriched sample $^{25}\text{MgAS}_{25_50}$, the small peak at $\delta_2 \approx 5$ ppm in the TQMAS spectrum indicates the presence of some six-coordinated Al, which is confirmed by our analysis of the MAS NMR spectrum. The amount of Al(VI) listed in Table IV may, however, be an overestimate because the presence of Al(VI) is not clear from the SATRAS data for this sample (Fig. 8). In general, for a given composition, the interaction parameters extracted from the ^{27}Al NMR spectra measured for the isotopically enriched ^{25}Mg vs $^{\text{nat}}\text{Mg}$ glasses are the same, within experimental errors.

3. ^{25}Mg MAS and static NMR

Figure 10 shows the solid-state ^{25}Mg MAS NMR spectra, acquired with a Hahn-echo sequence. The MAS NMR line shape for

TABLE IV. ^{27}Al spectral parameters for the samples containing ^{25}Mg vs $^{\text{nat}}\text{Mg}$. MAS-Czjzek: Parameters obtained from a deconvolution analysis of the ^{27}Al central-transition spectra using the Czjzek model for infinite spinning speed.^{41,45} average isotropic chemical shift (δ_{iso}), width of the Czjzek distribution σ , average quadrupolar coupling constant ($|C_Q|$) (defined in the sense of a modulus as per Ref. 56), relative intensity I , and average coordination number $\bar{n}_{\text{Al}}^{\text{O}}$. SATRAS: Average isotropic chemical shift (δ_{iso}) obtained from analysis of the spinning sidebands corresponding to satellite transitions. TQMAS: Average isotropic chemical shift (δ_{iso}) and second-order quadrupolar effect (P_Q) obtained from the center of gravity of the TQMAS cross peaks using Eqs. (14) and (15).

Glass	Site	MAS-Czjzek			I ($\pm 2\%$)	$\bar{n}_{\text{Al}}^{\text{O}}$	SATRAS	TQMAS	$\langle P_Q \rangle$ (± 0.1 MHz)
		$\langle \delta_{\text{iso}} \rangle$ (± 1 ppm)	σ (± 0.1 MHz)	$\langle C_Q \rangle$ (± 0.1 MHz)			$\langle \delta_{\text{iso}} \rangle$ (± 1 ppm)	$\langle \delta_{\text{iso}} \rangle$ (± 1 ppm)	
$^{\text{nat}}\text{MgAS}_{37.5_50}$	Al(IV)	63	4.0	7.9	84	4.16(7)	...	60	5.7
	Al(V)	38	4.1	8.1	16		...	31	3.2
$^{25}\text{MgAS}_{37.5_50}$	Al(IV)	64	3.9	7.9	83	4.17(7)	65	63	6.1
	Al(V)	38	4.1	8.1	17		38	36	4.7
$^{\text{nat}}\text{MgAS}_{25_50}$	Al(IV)	64	3.9	7.9	75	4.25(7)	...	59	7.1
	Al(V)	39	4.1	8.1	25		...	31	2.9
$^{25}\text{MgAS}_{25_50}$	Al(IV)	64	4.0	7.9	75	4.29(7)	68	63	6.1
	Al(V)	38	3.9	7.9	21		39	36	4.7
	Al(VI)	15	4.1	8.1	4		13	11	4.6
$^{\text{nat}}\text{MgAS}_{30_60}$	Al(IV)	62	3.7	7.3	81	4.19(7)	...	60	8.9
	Al(V)	37	4.3	7.9	19		...	30	6.4
$^{25}\text{MgAS}_{30_60}$	Al(IV)	61	3.9	7.9	80	4.20(7)	66	61	8.9
	Al(V)	38	4.6	9.1	20		42	30	6.4
$^{\text{nat}}\text{MgAS}_{20_60}$	Al(IV)	61	4.1	8.1	78	4.22(7)	...	60	6.1
	Al(V)	36	4.0	7.9	22		...	31	3.7
$^{25}\text{MgAS}_{20_60}$	Al(IV)	63	4.0	7.9	79	4.21(7)	65	61	6.2
	Al(V)	36	4.0	7.9	21		39	35	3.5

all the glasses is similar and is dominated by a wide chemical shift dispersion due to a distribution of quadrupolar coupling strengths whose effects upon the NMR line shape can be treated in the regime of second-order perturbation theory. The entire line shape could

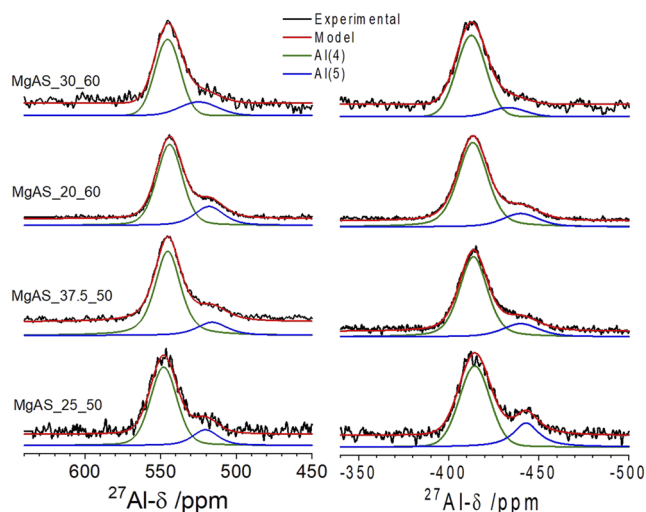


FIG. 8. The ^{27}Al SATRAS data for the isotopically enriched aluminosilicate glasses. For each glass composition, the third spinning sidebands on each side of the peak for the central-transition are shown. The spectra were deconvoluted using DMfit.³⁹ Note that the improved resolution helps to distinguish between the four- and five-coordinated Al species.

be successfully modeled using a Czjzek distribution, implemented within the ssNake program.⁴⁵ The simulations were performed assuming the finite MAS rate regime, where 16 spinning sidebands were simulated by the Carousel averaging approach implemented in the software. An unconstrained fitting approach was used to determine the best-fit parameters. A Gaussian line-broadening (LB) parameter was employed to account for a distribution of isotropic chemical shifts.

The simulation parameters are listed in Table V, where the mean chemical shift takes a value in the range from 12 to 28 ppm. There is imprecision in the value of this parameter that originates from the large linewidth. In crystalline compounds, a chemical shift between zero and 30 ppm relative to aqueous MgCl_2 solution is typical of magnesium in a six-coordinated environment Mg(VI), whereas a chemical shift of 40–80 ppm is typical of magnesium in a four-coordinated environment Mg(IV).⁹ The results therefore suggest that the Mg^{2+} ions in the different glasses are predominantly six-coordinated. As discussed in Sec. V, this interpretation is in stark contrast to the results found in the diffraction work.

We have also recorded the static ^{25}Mg NMR spectrum for the isotopically enriched sample $^{25}\text{MgAS}_{30_60}$ using the WURST-CPMG pulse sequence with a stepwise acquisition, with the carrier frequency varied in steps of 360 kHz (10 000 ppm). The spectrum is shown in Fig. 11 on two different scales, showing the central-transition line (left column) and the spikelet patterns visible on the high-frequency side of the central resonance (right column), which can be attributed to the satellite transition manifold. The line shape (spikelet envelope) is broadly consistent with a simulation based on the parameters obtained from the fit to the MAS NMR spectrum.

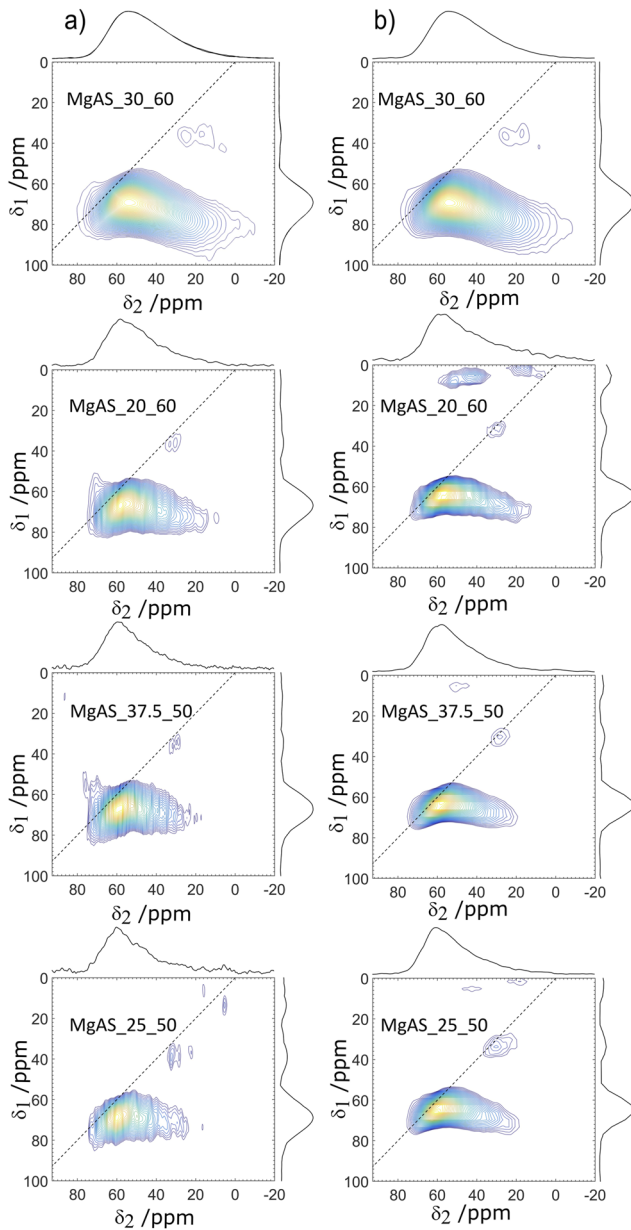


FIG. 9. The ^{27}Al TQMAS NMR spectra for the aluminosilicate glasses containing either (a) isotopically enriched ^{25}Mg or (b) magnesium with its natural isotopic abundance. Broken lines correspond to the diagonal of the 2D spectra where the $\delta_1:\delta_2$ ratio is 1:1.

C. Neutron diffraction with isotope substitution

The scattering lengths used in the analysis of the neutron diffraction data for the glassy materials were $b_{\text{Al}} = 3.449(5)$ fm, $b_{\text{Si}} = 4.1491(10)$ fm, $b_{\text{O}} = 5.803(4)$ fm,²⁶ $b_{\text{nat,Mg}} = 5.375(4)$ fm (Table II), and taking into account the isotopic enrichment, $b_{^{25}\text{Mg}} = 3.739(12)$ fm for diopside, $b_{^{25}\text{Mg}} = 3.745(10)$ fm for enstatite, and $b_{^{25}\text{Mg}} = 3.729(12)$ fm for the MgAS glasses. The measured neutron

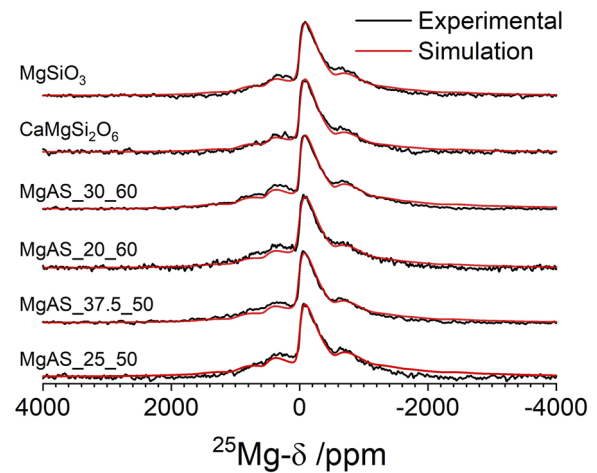


FIG. 10. The ^{25}Mg MAS NMR spectra for the ^{25}Mg enriched magnesium silicate and aluminosilicate glasses. The measured datasets, obtained by rotor-synchronized Hahn spin echo acquisition at a rotor frequency of 20.0 kHz (acquisition after two rotor cycles), are shown by black curves and the simulations obtained from a distribution of electric field gradients given by the Czjzek model are shown by red curves. The datasets for diopside and enstatite glasses are adopted from Ref. 8.

TABLE V. Deconvolution analysis for the central transition of the ^{25}Mg MAS NMR spectra, measured for the isotopically enriched glasses at a finite spinning rate of 20 kHz, using the Czjzek model as implemented in the ssNake software.⁴⁵ The fitted parameters were unconstrained. LB is a line-broadening parameter corresponding to the convolution of the calculated spectrum with a Gaussian function. The datasets for diopside and enstatite glasses are taken from Ref. 8.

Glass	$\langle \delta_{\text{iso}} \rangle$ (± 5 ppm)	σ (± 0.2 MHz)	$\langle C_Q \rangle$ (± 0.4 MHz)	LB (± 0.5 kHz)
Diopside	13	4.2	8.3	2.0
Enstatite	13	4.4	8.6	3.0
MgAS_37.5_50	28	4.5	8.9	2.5
MgAS_25_50	12	4.5	8.9	3.0
MgAS_30_60	13	4.7	9.3	2.0
MgAS_20_60	20	4.5	8.9	2.5

total structure factors are shown in Fig. 12. The contrast in shape with the x-ray total structure factors (Fig. 1) reflects a difference in weighting of the $S_{\alpha\beta}(k)$ functions.

The measured $\Delta F_{\text{Mg}}(k)$ functions are illustrated in Fig. 13 and show contrast between the total structure factors measured for each glass. The first peak in the corresponding $\Delta D'_{\text{Mg}}(r)$ functions (Fig. 14) is attributed to nearest-neighbor Mg–O correlations and encompasses typical Mg–O nearest-neighbor distances. For example, the Mg–O bond length is 1.923(1) Å for the MgO_4 polyhedra of crystalline MgAl_2O_4 ,¹ is in the range 2.09(9)–2.31(38) Å for the MgO_6 polyhedra of crystalline MgO ,² MgSiO_3 ,³ $\beta\text{-Mg}_2\text{SiO}_4$,⁴ and $\text{Mg}_{0.5}\text{AlSiO}_4$,⁵ and is 2.27(8) Å for the MgO_8 polyhedra of crystalline $\text{Mg}_3\text{Al}_2\text{Si}_3\text{O}_{12}$.⁶ Unlike crystalline MgO (Fig. 4), the first Mg–O peak is broad and asymmetric and was therefore represented by two

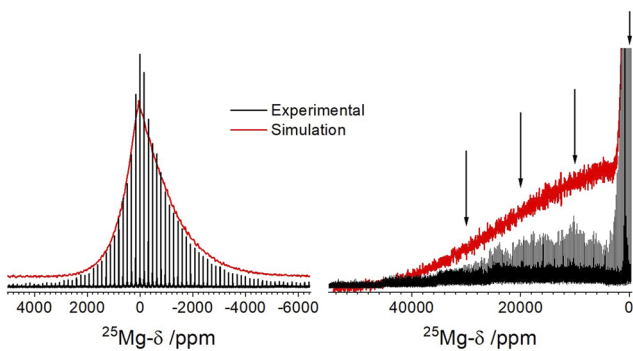


FIG. 11. Left column: The static ^{25}Mg WURST-CPMG spikelet spectra for the isotopically enriched sample $^{25}\text{MgAS}_{30_60}$ (black curve) and the simulation using the Czjzek distribution (red curve) obtained by fixing the parameter values at those obtained from the simulations of the ^{25}Mg MAS NMR spectra (Fig. 10). Right column: Same spectrum and fit as in the left column but on an expanded scale, showing the resonances corresponding to the ^{25}Mg satellite transitions. The arrows indicate the resonance offsets used for the stepwise acquisition of the wideline spectrum.

Gaussian functions. A third Gaussian function was used in the fitting procedure to constrain the high- r side of these Mg–O peaks.

The fitted $\Delta D'_{\text{Mg}}(r)$ functions are shown in Fig. 14. The fitted parameters are listed in Table VI along with the weighted mean bond distance given by

$$\bar{r}_{\text{MgO}} = \frac{\int_{r_1}^{r_2} dr r g_{\text{MgO}}(r)}{\int_{r_1}^{r_2} dr g_{\text{MgO}}(r)}, \quad (18)$$

where $g_{\text{MgO}}(r)$ was obtained from the sum of the Gaussian functions fitted to the first peak and r_1 and r_2 define the overall extent of this peak. For each glass, the overall Mg–O coordination number $\bar{n}_{\text{Mg}}^{\text{O}}(\text{sum})$ obtained from the fitting procedure is in agreement with the value found directly from $\Delta D'_{\text{Mg}}(r)$ by using Eq. (10) to integrate over the first peak after the application of a Lorch modification function.^{59,60} The value of $\bar{n}_{\text{Mg}}^{\text{O}}(\text{sum}) = 4.46(4)$ for enstatite glass is in accord with the value of 4.50(2) measured previously using neutron diffraction with magnesium isotope substitution.¹⁶

The measured $\Delta F(k)$ functions for the enstatite, diopside, and MgAS glasses are shown in Fig. 15 and the corresponding $\Delta D'(r)$ functions are shown in Fig. 16.

For enstatite glass, the first peak in $\Delta D'(r)$ originates solely from Si–O correlations and was fitted to a single Gaussian function. A second Gaussian function was used to fit the O–O correlations, which are expected at a mean distance of $\bar{r}_{\text{OO}} = \sqrt{8/3} \bar{r}_{\text{SiO}} \approx 2.65 \text{ \AA}$ for a tetrahedral SiO_4 unit, where \bar{r}_{SiO} is the mean intra-tetrahedral Si–O bond distance. The fitted function is shown in Fig. 16 and the fitted parameters are listed in Table VII. The diffraction results are consistent with $\bar{n}_{\text{Si}}^{\text{O}} = 4$, as found from ^{29}Si MAS NMR experiments on enstatite glass.^{8,61,62}

For the MgAS glasses, there is also a contribution to the first peak in $\Delta D'(r)$ from the Al–O correlations, which causes this peak to become more asymmetric as the alumina content of the glass increases (Fig. 16). These correlations were represented by an additional Gaussian function with $\bar{n}_{\text{Al}}^{\text{O}}$ set to the value found from the

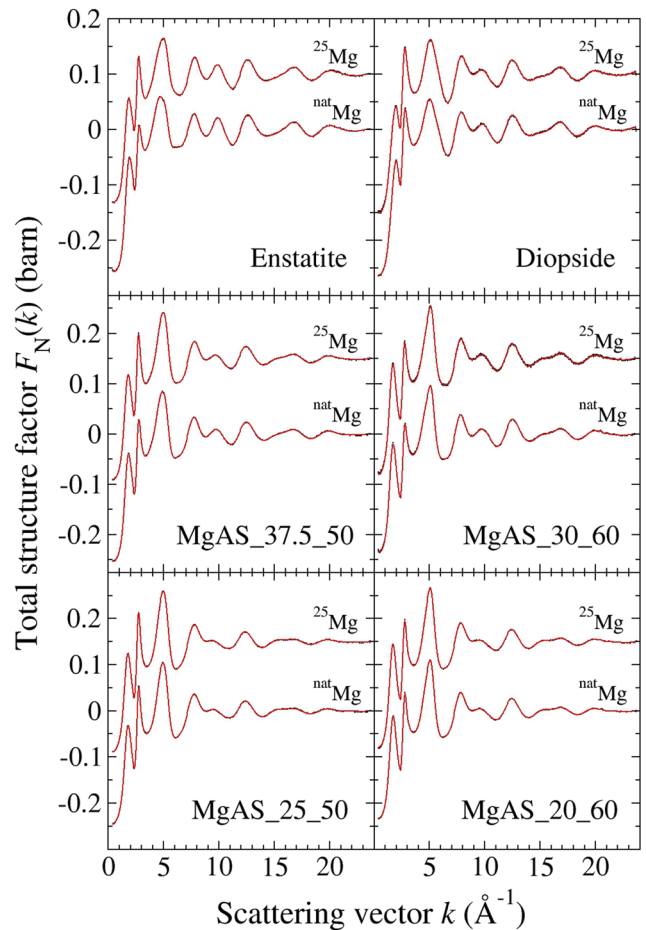


FIG. 12. The measured $F_N(k)$ functions for the enstatite, diopside, and MgAS glasses containing either $^{\text{nat}}\text{Mg}$ or ^{25}Mg . For each glass, the points with black vertical error bars give the measured function and the red curve gives the back Fourier transform of the corresponding $D'_N(r)$ function (Figs. 18 and 19) after the low- r oscillations, below the distance of closest approach between two atoms, are set to the theoretical density-line limit. For each glass, the vertical error bars are smaller than the curve thickness at most k values.

^{27}Al MAS NMR experiments (Table IV). There is little change to aluminum speciation with the glass composition, so there is little change to the mean Al–O distance \bar{r}_{AlO} (Table VII).

For diopside glass, in addition to the contributions to $\Delta D'(r)$ from nearest-neighbor Si–O and O–O correlations, there is also a contribution from nearest-neighbor Ca–O correlations. To help assess their effect, the $D'_X(r)$ functions were fitted using (i) a single Gaussian function for the nearest-neighbor Si–O correlations with the coordination number set at the value $\bar{n}_{\text{Si}}^{\text{O}} = 4$ found from ^{29}Si MAS NMR experiments,^{8,63} (ii) two Gaussian functions for the Mg–O correlations with the coordination numbers set at the values found from fitting $\Delta D'_{\text{Mg}}(r)$ (Table VI), and (iii) single Gaussian functions for both the Ca–O and O–O correlations. The x-ray datasets were used because of their enhanced sensitivity to the calcium pair-correlation functions: The atomic number of Ca ($Z = 20$)

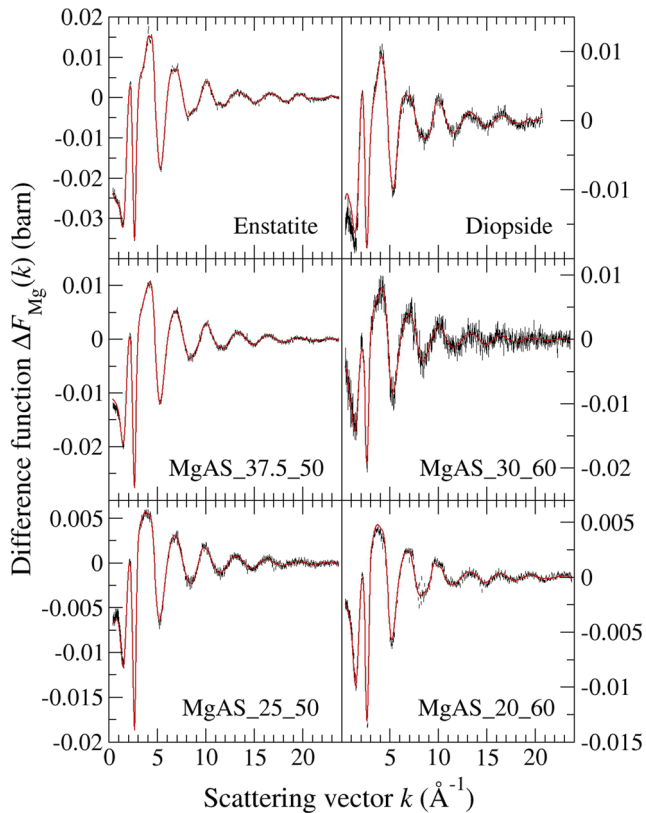


FIG. 13. The measured $\Delta F_{\text{Mg}}(k)$ functions for the enstatite, diopside, and MgAS glasses. For each glass, the points with black vertical error bars give the measured function and the red curve gives the back Fourier transform of the corresponding $\Delta D'_{\text{Mg}}(r)$ function (Fig. 14) after the low- r oscillations, below the distance of closest approach between two atoms, are set to the theoretical density-line limit.

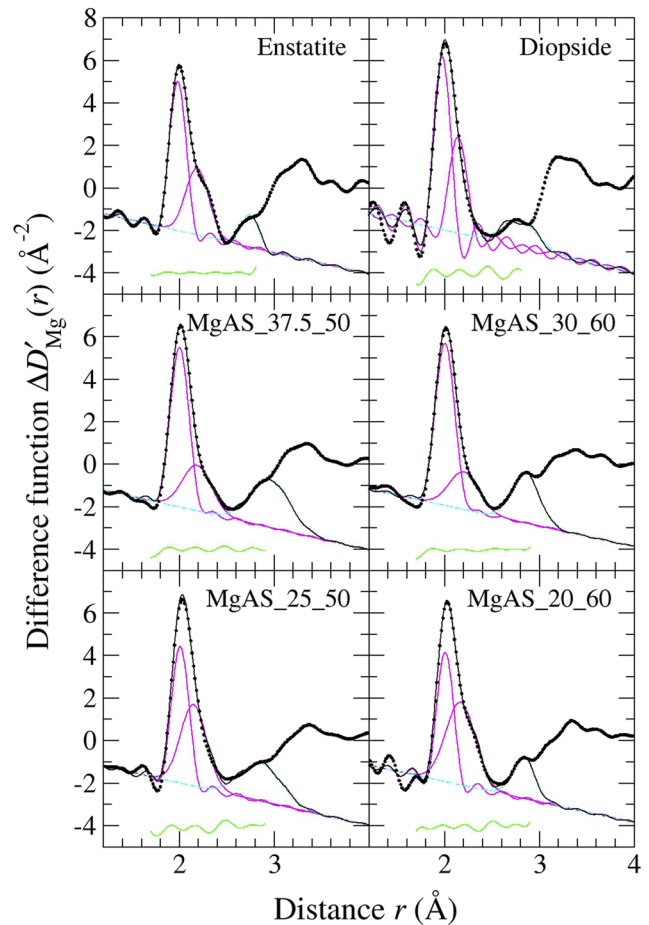


FIG. 14. The fitted $\Delta D'_{\text{Mg}}(r)$ functions for the enstatite, diopside, and MgAS glasses. In each panel, the black solid circles give the measured function, the black solid curve gives the fitted function, and the other curves show the contributions from the Mg-O (magenta solid curves) and Mg- β ($\beta \neq \text{O}$) (cyan broken curve) correlations. The latter was introduced to constrain the peaks fitted at smaller r -values. The displaced green solid curve shows the residual.

TABLE VI. The Mg-O peak parameters obtained from the fitted $\Delta D'_{\text{Mg}}(r)$ functions for the diopside, enstatite, and MgAS glasses. The error associated with $r_{\text{MgO},i}$ is typically $\pm 0.004 \text{ \AA}$ ($i = 1$) or $\pm 0.008 \text{ \AA}$ ($i = 2$). The error associated with $\sigma_{\text{MgO},i}$ is typically $\pm 0.004 \text{ \AA}$ ($i = 1$) or $\pm 0.007 \text{ \AA}$ ($i = 2$). The error associated with $\bar{n}_{\text{Mg},i}^{\text{O}}$ ($i = 1$ or 2) is typically ± 0.03 . The weighted mean Mg-O distance \bar{r}_{MgO} was obtained from the fitted peaks by applying Eq. (18) and has a typical error of $\pm 0.008 \text{ \AA}$. The overall Mg-O coordination number $\bar{n}_{\text{Mg}}^{\text{O}}(\text{sum})$ was obtained using the full precision of the measurements and has a typical error of ± 0.04 . The goodness-of-fit parameter R_{χ} is also given.

Glass	First peak			Second peak			Overall		
	$r_{\text{MgO},1} (\text{\AA})$	$\sigma_{\text{MgO},1} (\text{\AA})$	$\bar{n}_{\text{Mg},1}^{\text{O}}$	$r_{\text{MgO},2} (\text{\AA})$	$\sigma_{\text{MgO},2} (\text{\AA})$	$\bar{n}_{\text{Mg},2}^{\text{O}}$	$\bar{r}_{\text{MgO}} (\text{\AA})$	$\bar{n}_{\text{Mg}}^{\text{O}}(\text{sum})$	R_{χ}
Diopside	1.975	0.050	2.61	2.143	0.069	1.80	2.036	4.40	0.074
Enstatite	1.984	0.077	2.59	2.188	0.120	1.87	2.056	4.46	0.022
MgAS_37.5_50	2.003	0.092	3.17	2.186	0.152	1.59	2.051	4.76	0.042
MgAS_25_50	2.010	0.080	2.43	2.150	0.136	2.47	2.070	4.90	0.071
MgAS_30_60	2.004	0.098	3.40	2.204	0.157	1.36	2.047	4.77	0.040
MgAS_20_60	2.007	0.073	2.17	2.168	0.156	2.91	2.086	5.07	0.044

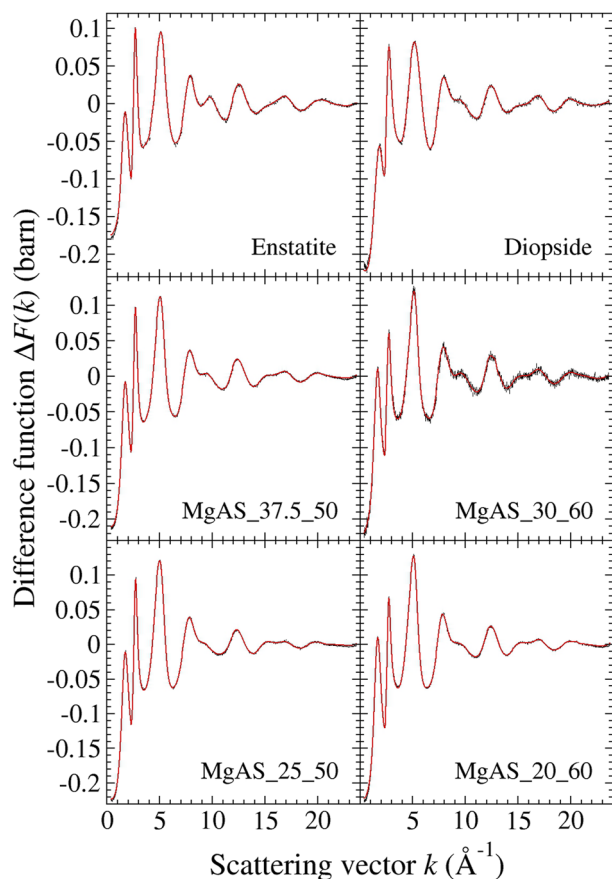


FIG. 15. The measured $\Delta F(k)$ functions for the enstatite, diopside, and MgAS glasses. For each glass, the points with black vertical error bars give the measured function and the red curve gives the back Fourier transform of the corresponding $\Delta D'(r)$ function (Fig. 16) after the low- r oscillations, below the distance of closest approach between two atoms, are set to the theoretical density-line limit.

is larger than for the other chemical species present in the glass. The fitted function is shown in Fig. 17 and the fitted parameters are listed in Tables VIII and IX. A Ca–O coordination number of 5.01–5.06 was obtained with an associated bond distance of 2.353(5)–2.357(5) Å. The neutron $\Delta D'(r)$ function (Fig. 16) was then fitted following the procedure adopted for enstatite, but with an additional Gaussian function for the Ca–O correlations and $\bar{n}_{\text{Ca}}^{\text{O}}$ constrained to the range of values found in the x-ray diffraction work. The results give $\bar{n}_{\text{Ca}}^{\text{O}} \approx 5$ with $\bar{r}_{\text{CaO}} = 2.374(5)$ Å (Table VII), which compare to $\bar{n}_{\text{Ca}}^{\text{O}} = 8$ for crystalline diopside with Ca–O distances in the range 2.352–2.717 Å.⁶⁴ The $\bar{n}_{\text{Ca}}^{\text{O}}$ value for the glass may, however, be larger than indicated if the distribution of nearest neighbors is asymmetric, as found for the coordination environment of magnesium in the same material.

As a check on the internal consistency of the neutron diffraction datasets, each $D'_N(r)$ function was fitted using the results from the difference functions as starting parameters, subject to the constraints that $\bar{n}_{\text{Si}}^{\text{O}} = 4$, $\bar{n}_{\text{Al}}^{\text{O}}$ is given by the value found from the ²⁷Al

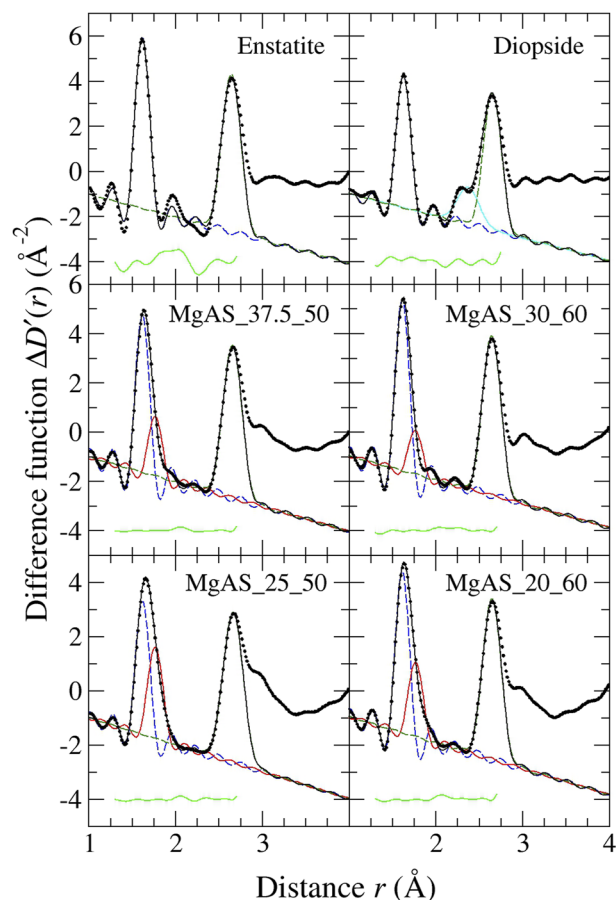


FIG. 16. The fitted $\Delta D'(r)$ functions for the enstatite, diopside, and MgAS glasses. In each panel, the black solid circles give the measured function, the black solid curve gives the fitted function, and the other curves show the contributions from the Si–O (blue broken curve), Al–O (red solid curve, only for the MgAS glasses), O–O (green broken curve), and Ca–O (cyan solid curve, only for diopside) correlations. The displaced green solid curve shows the residual. The O–O correlations were introduced to constrain the peaks fitted at smaller r -values.

MAS NMR experiments, and $\bar{n}_{\text{Mg}}^{\text{O}}$ for each peak is given by the value found from the corresponding $\Delta D'_{\text{Mg}}(r)$ function. For each glass composition, the $D'_N(r)$ functions (Figs. 18 and 19) could be represented with only minor adjustments to the peak positions (on average $\lesssim 0.6\%$) and peak widths (on average $\lesssim 3.9\%$ for σ_{SiO} , σ_{AlO} and $\sigma_{\text{MgO},1}$ vs $\lesssim 6.1\%$ for $\sigma_{\text{MgO},2}$) (Tables X and XI). The fitted functions demonstrate the benefit of using neutron diffraction with magnesium isotope substitution in removing the overlap between (i) the Mg–O and Ca–O nearest-neighbor correlations for diopside and (ii) the Mg–O and Al–O correlations for the MgAS glasses.

Finally, the $D'_X(r)$ functions for the MgAS glasses were fitted using the same strategy as for the neutron total pair-distribution functions, i.e., by setting $\bar{n}_{\text{Si}}^{\text{O}} = 4$, $\bar{n}_{\text{Al}}^{\text{O}}$ to the value measured by ²⁷Al MAS NMR, and $\bar{n}_{\text{Mg}}^{\text{O}}$ for each of the Gaussian peaks to the

TABLE VII. The Si–O and Al–O peak parameters obtained from the fitted $\Delta D'(r)$ functions for the diopside, enstatite, and MgAS glasses. Fixed parameters are marked with an asterisk, where the $\bar{n}_{\text{Al}}^{\text{O}}$ values were obtained from the ^{27}Al MAS NMR experiments (Table IV). The errors associated with \bar{r}_{SiO} and σ_{SiO} are typically ± 0.003 and ± 0.005 Å, respectively, and the errors associated with \bar{r}_{AlO} and σ_{AlO} are typically ± 0.005 Å. The goodness-of-fit parameter R_{χ} is also given.

Glass	\bar{r}_{SiO} (Å)	σ_{SiO} (Å)	$\bar{n}_{\text{Si}}^{\text{O}}$	\bar{r}_{AlO} (Å)	σ_{AlO} (Å)	$\bar{n}_{\text{Al}}^{\text{O}}$	R_{χ}
Diopside ^a	1.627	0.059	4.00*	0.063
Enstatite	1.617	0.059	4.00*	0.115
MgAS_37.5_50	1.618	0.045	4.00*	1.765	0.051	4.17*	0.021
MgAS_25_50	1.620	0.051	4.00*	1.766	0.072	4.27*	0.021
MgAS_30_60	1.614	0.048	4.00*	1.765	0.053	4.20*	0.028
MgAS_20_60	1.614	0.047	4.00*	1.768	0.065	4.22*	0.026

^aNearest-neighbor Ca–O correlations: $\bar{r}_{\text{CaO}} = 2.374(5)$ Å, $\sigma_{\text{CaO}} = 0.123(6)$ Å and $\bar{n}_{\text{Ca}}^{\text{O}} = 5.01(5)$.

value found from $\Delta D'_{\text{Mg}}(r)$. Again, the measured $D'_{\chi}(r)$ functions (Fig. 17) could be fitted with only minor adjustments to the peak widths and positions (Tables VIII and IX). As compared to the $D'_{\text{N}}(r)$ functions, there is increased overlap between the Mg–O and O–O correlations, which emphasizes the benefit of using neutron diffraction with isotope substitution to gain unambiguous information on the coordination environment of magnesium.

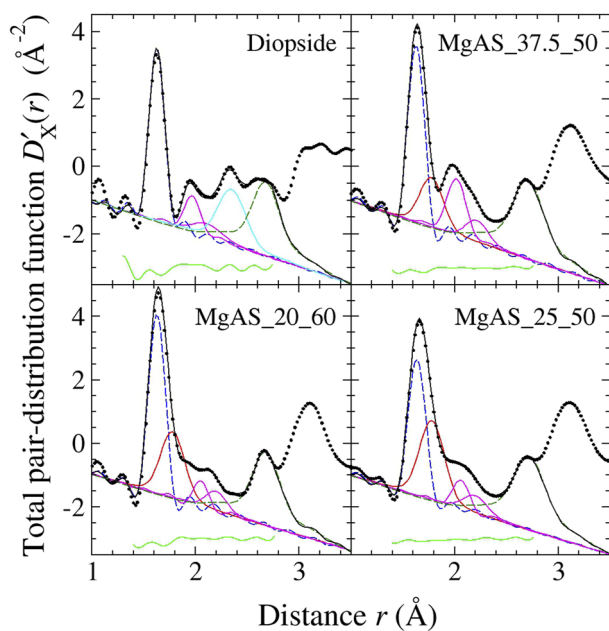


FIG. 17. The fitted $D'_{\chi}(r)$ functions for the glasses investigated by x-ray diffraction. In each panel, the black solid circles give the function measured for the sample containing ^{25}Mg , the black solid curve gives the fitted function, and the other curves show the contributions from the Si–O (blue broken curve), Al–O (red solid curve, only for the MgAS glasses), O–O (green broken curve), and Ca–O (cyan solid curve, only for diopside) correlations. The displaced green solid curve shows the residual. The O–O correlations were introduced to constrain the peaks fitted at smaller r -values.

V. DISCUSSION

In all the investigated glasses, the measured $\Delta D'_{\text{Mg}}(r)$ functions show that the local coordination environment of magnesium is characterized by a broad and asymmetric distribution of Mg–O distances (Fig. 14), indicating a wide distribution of coordination environments for the Mg^{2+} ions. This finding is consistent with molecular dynamics studies of enstatite glass where Mg^{2+} is found to be four-, five-, or six-coordinated, and the distortion of the polyhedral units is quantified using an orientational order parameter.¹⁴ The variety leads to a broad distribution of electric field gradient components at the magnesium position, as inferred from ^{25}Mg solid-state NMR experiments on the diopside and enstatite glasses⁸ and confirmed by the asymmetry of the spectra measured for the MgAS glasses in this work. It follows from the diffraction study that the majority of Mg^{2+} ions are not six-coordinated, in contrast to the expectation originating from the chemical shifts observed in unconstrained fits to the ^{25}Mg MAS NMR spectra (Table V) and in contrast to the findings of previous work using ^{25}Mg MAS^{65–67} or TQMAs NMR spectroscopy^{68,69} on the same or related silicate glasses.

At the heart of this issue is the strong effect on the solid-state ^{25}Mg NMR spectra of a wide distribution of quadrupolar coupling strengths. This distribution reflects the variation in local magnesium coordination environments and results in excessive loss of site-specific resolution in the measured spectra. In the case of enstatite glass, for example, the MAS NMR spectrum could be adequately fitted by constraining the chemical shift to 50 ppm, which is typical of four-coordinated Mg species.⁸ A satisfactory fit to the spectrum could also be obtained by assuming a 1:1 superposition of Mg species with chemical shifts of 13 and 50 ppm to mimic magnesium in a five-coordinated environment. The present study confirms that, for the ^{25}Mg MAS NMR spectra collected at 14.1 T with a magic angle spinning rate of 20 kHz, the distribution of Mg^{2+} coordination numbers cannot be revealed. In future work, this issue might be addressed by much higher magnetic flux densities (28.2 T) and spinning speeds (>50 kHz). In the end, the ultimate resolution limit will be dominated by the width of the distribution of the isotropic chemical shifts associated with each of the Mg coordination states, such as Mg(IV), Mg(V), and

TABLE VIII. The Si–O and Al–O peak parameters obtained from the fitted $D'_X(r)$ functions for diopside and several of the MgAS glasses. Fixed parameters are marked with an asterisk, where the $\bar{n}_{\text{Al}}^{\text{O}}$ values were obtained from the ^{27}Al MAS NMR experiments (Table IV). The errors associated with \bar{r}_{SiO} and σ_{SiO} are typically ± 0.001 Å and the errors associated with \bar{r}_{AlO} and σ_{AlO} are typically ± 0.003 Å. The goodness-of-fit parameter R_X is also given.

Glass	\bar{r}_{SiO} (Å)	σ_{SiO} (Å)	$\bar{n}_{\text{Si}}^{\text{O}}$	\bar{r}_{AlO} (Å)	σ_{AlO} (Å)	$\bar{n}_{\text{Al}}^{\text{O}}$	R_X
^{nat} Diopside ^a	1.625	0.060	4.00*	0.095
²⁵ Diopside ^b	1.626	0.065	4.00*	0.116
^{nat} MgAS_37.5_50	1.626	0.063	4.00*	1.780	0.089	4.17*	0.053
²⁵ MgAS_37.5_50	1.630	0.067	4.00*	1.780	0.113	4.17*	0.039
^{nat} MgAS_25_50	1.639	0.074	4.00*	1.784	0.120	4.27*	0.036
²⁵ MgAS_25_50	1.643	0.075	4.00*	1.785	0.127	4.27*	0.038
^{nat} MgAS_20_60	1.628	0.067	4.00*	1.780	0.116	4.22*	0.062
²⁵ MgAS_20_60	1.631	0.070	4.00*	1.779	0.125	4.22*	0.061

^aNearest-neighbor Ca–O correlations: $\bar{r}_{\text{CaO}} = 2.357(5)$ Å, $\sigma_{\text{CaO}} = 0.137(4)$ Å and $\bar{n}_{\text{Ca}}^{\text{O}} = 5.06(12)$.

^bNearest-neighbor Ca–O correlations: $\bar{r}_{\text{CaO}} = 2.353(5)$ Å, $\sigma_{\text{CaO}} = 0.142(3)$ Å and $\bar{n}_{\text{Ca}}^{\text{O}} = 5.01(13)$.

TABLE IX. The Mg–O peak parameters obtained from the fitted $D'_X(r)$ functions for diopside and several of the MgAS glasses. Fixed parameters are marked by an asterisk and were obtained from the measured $\Delta D'_{\text{Mg}}(r)$ functions (Table VI). The errors associated with $r_{\text{MgO},i}$ and $\sigma_{\text{MgO},i}$ ($i = 1, 2$) are typically ± 0.005 and ± 0.007 Å, respectively. The weighted mean Mg–O distance \bar{r}_{MgO} was obtained from the fitted peaks by applying Eq. (18) and has a typical error of ± 0.008 Å.

Glass	First peak			Second peak			Overall	
	$r_{\text{MgO},1}$ (Å)	$\sigma_{\text{MgO},1}$ (Å)	$\bar{n}_{\text{Mg},1}^{\text{O}}$	$r_{\text{MgO},2}$ (Å)	$\sigma_{\text{MgO},2}$ (Å)	$\bar{n}_{\text{Mg},2}^{\text{O}}$	\bar{r}_{MgO} (Å)	$\bar{n}_{\text{Mg}}^{\text{O}}$ (sum)
^{nat} Diopside	1.976	0.073	2.61*	2.092	0.116	1.80*	2.016	4.40*
²⁵ Diopside	1.970	0.071	2.61*	2.112	0.134	1.80*	2.019	4.40*
^{nat} MgAS_37.5_50	2.015	0.076	3.17*	2.208	0.089	1.59*	2.069	4.76*
²⁵ MgAS_37.5_50	2.020	0.088	3.17*	2.218	0.107	1.59*	2.074	4.76*
^{nat} MgAS_25_50	2.063	0.068	2.43*	2.200	0.114	2.47*	2.124	4.90*
²⁵ MgAS_25_50	2.072	0.074	2.43*	2.197	0.125	2.47*	2.127	4.90*
^{nat} MgAS_20_60	2.053	0.050	2.17*	2.200	0.099	2.91*	2.129	5.07*
²⁵ MgAS_20_60	2.063	0.064	2.17*	2.200	0.114	2.91*	2.133	5.07*

Mg(VI). If these widths are much larger than the differences between the respective average shifts of these coordination environments, no peak resolution will be observable, no matter how high the magnetic field strength. Furthermore, other resolution limitations associated with chemical shift anisotropy could enter at higher magnetic field strengths.

The Mg–O coordination number increases with the weighted mean Mg–O distance \bar{r}_{MgO} as the alumina content is increased along either the 50 or 60 mol.% silica tie-line (Table VI). For example, along the 50 mol.% silica tie-line, $\bar{n}_{\text{Mg}}^{\text{O}} = 4.46(4)$ for enstatite, which corresponds to the alumina free end-member composition, and increases as magnesia is replaced by alumina to reach the value $\bar{n}_{\text{Mg}}^{\text{O}} = 4.90(4)$ in MgAS_25_50 glass when $R = 1$. In contrast, Guignard and Cormier⁷⁰ applied the reverse Monte Carlo method to the neutron and x-ray diffraction datasets measured for four different MgAS glasses along the 50 mol.% silica tie-line and found little change from $\bar{n}_{\text{Mg}}^{\text{O}} \approx 5.1(1)$ with the glass composition.

It should be noted that the $\bar{n}_{\text{Mg}}^{\text{O}}$ values reported in this work account for the area under the first peak and shoulder in the

measured $\Delta D'_{\text{Mg}}(r)$ functions, extending to the first minimum at $r_{\text{min}} \approx 2.5$ Å. More remote oxygen atoms may, however, produce a large- r tail to $g_{\text{MgO}}(r)$ that contributes toward the Mg- β peak near 2.8 Å in $\Delta D'_{\text{Mg}}(r)$ (Fig. 14). These oxygen neighbors may also affect the ^{25}Mg NMR chemical shifts. In the case of enstatite glass, the measured $\Delta D'_{\text{Mg}}(r)$ function does not suggest a pronounced tail, as emphasized by plotting the function

$$\Delta G_{\text{Mg}}(r) = (2c_{\text{Mg}}\Delta b_{\text{Mg}}/B) \sum_{\alpha \neq \text{Mg}} c_{\alpha} b_{\alpha} g_{\text{Mg}\alpha}(r) + \left[c_{\text{Mg}}^2 \left(b_{\text{nat Mg}}^2 - b_{\text{Mg}}^2 \right) / B \right] g_{\text{MgMg}}(r), \quad (19)$$

which takes the value of zero at r_{min} (Fig. 20). Nevertheless, molecular dynamics simulations of enstatite glass using an aspherical ion model¹⁴ do show a tail on the high- r side of the first peak in $g_{\text{MgO}}(r)$ and contributions toward the Mg- β peak from the Mg–O, Mg–Si, and Mg–Mg correlations (Fig. 20).

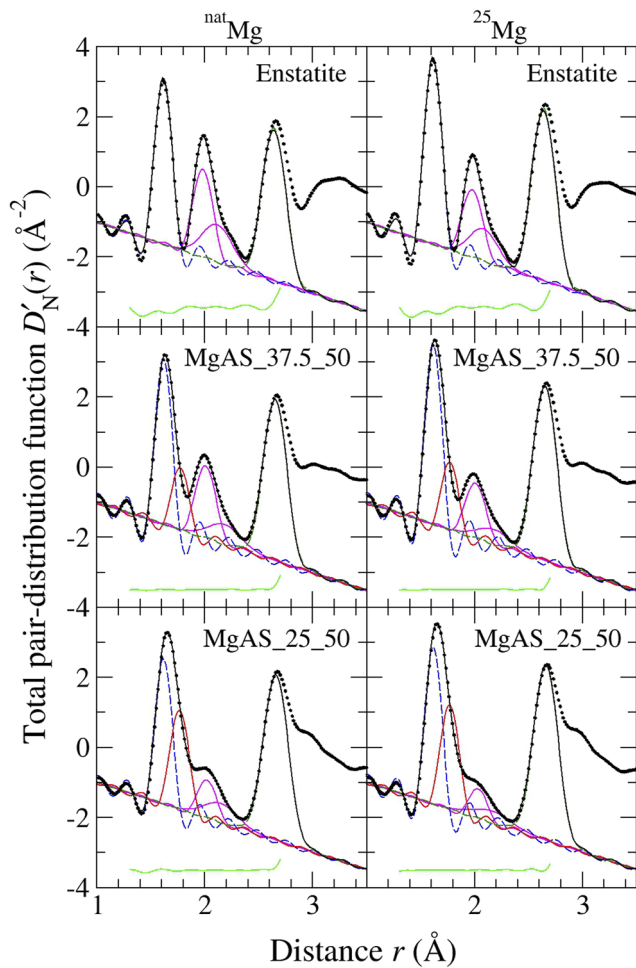


FIG. 18. The fitted $D'_N(r)$ functions for enstatite and two MgAS glasses along the 50 mol. % silica tie-line for the samples containing either ^{nat}Mg (left column) or ^{25}Mg (right column). In each panel, the black solid circles give the measured function, the black solid curve gives the fitted function, and the other curves show the contributions from the Si–O (blue broken curve), Al–O (red solid curve, only for the MgAS glasses), Mg–O (magenta solid curves), and O–O (green broken curve) correlations. The displaced green solid curve shows the residual. The O–O correlations were introduced to constrain the peaks fitted at smaller r -values.

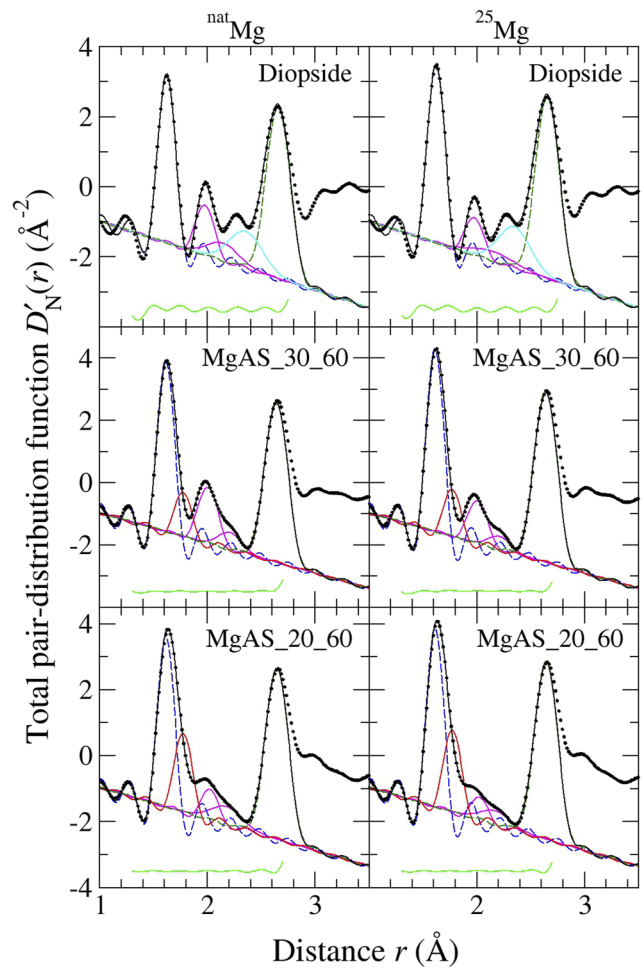


FIG. 19. The fitted $D'_N(r)$ functions for diopside and two MgAS glasses along the 60 mol. % silica tie-line for the samples containing either ^{nat}Mg (left column) or ^{25}Mg (right column). In each panel, the black solid circles give the measured function, the black solid curve gives the fitted function, and the other curves show the contributions from the Si–O (blue broken curve), Al–O (red solid curve, only for the MgAS glasses), Mg–O (magenta solid curves), Ca–O (cyan solid curve, only for diopside), and O–O (green broken curve) correlations. The displaced green solid curve shows the residual. The O–O correlations were introduced to constrain the peaks fitted at smaller r -values.

In diopside and the other investigated glasses, Mg–O coordination numbers of less than five indicate the presence of four-coordinated Mg^{2+} ions. For example, if only four- and five-coordinated species are present in the glass structure, and if $f_{\text{Mg(IV)}}$ denotes the fraction of four-coordinated Mg^{2+} ions, it follows that the mean coordination number $\bar{n}_{\text{Mg}}^{\text{O}} = 4f_{\text{Mg(IV)}} + 5[1 - f_{\text{Mg(IV)}}]$. In the case of diopside, the measured value $\bar{n}_{\text{Mg}}^{\text{O}} = 4.40(4)$ then implies that 60% of the magnesium is four-coordinated.

There is, however, no evidence in support of four-coordinated magnesium adopting a network-forming role (Sec. 1). For example, the Q^n speciation found from ^{29}Si MAS NMR experiments on glassy diopside,^{8,63} enstatite,^{8,61,62} and wollastonite (CaSiO_3)^{63,71,72}

is similar for all three materials, giving a mean value $\langle n \rangle \approx 2$. Hence, there is nothing to distinguish between the structural roles played by Ca^{2+} , which is usually regarded as a network modifier, and Mg^{2+} . Additionally, the entropy of mixing found from viscosity measurements on the pyroxene CaSiO_3 – MgSiO_3 , garnet $\text{Ca}_3\text{Al}_2\text{Si}_3\text{O}_{12}$ – $\text{Mg}_3\text{Al}_2\text{Si}_3\text{O}_{12}$, and anorthite $\text{CaAl}_2\text{Si}_2\text{O}_8$ – $\text{MgAl}_2\text{Si}_2\text{O}_8$ systems, in which Ca^{2+} was systematically replaced by Mg^{2+} , is consistent with an ideal mixing hypothesis for these cations.^{73,74} The measurements do not, therefore, indicate any substantial difference between the structural roles played by the Ca^{2+} and Mg^{2+} ions.

TABLE X. The Si–O and Al–O peak parameters obtained from the fitted $D'_N(r)$ functions measured for diopside, enstatite, and the MgAS glasses. Fixed parameters are marked with an asterisk, where the $\bar{n}_{\text{Al}}^{\text{O}}$ values were obtained from the ^{27}Al MAS NMR experiments (Table IV). The errors associated with \bar{r}_{SiO} and σ_{SiO} are typically ± 0.003 and ± 0.005 Å, respectively, and the errors associated with \bar{r}_{AlO} and σ_{AlO} are typically ± 0.005 Å. The goodness-of-fit parameter R_χ is also given.

Glass	\bar{r}_{SiO} (Å)	σ_{SiO} (Å)	$\bar{n}_{\text{Si}}^{\text{O}}$	\bar{r}_{AlO} (Å)	σ_{AlO} (Å)	$\bar{n}_{\text{Al}}^{\text{O}}$	R_χ
^{nat} Diopside ^a	1.622	0.058	4.00*	0.064
²⁵ Diopside ^b	1.624	0.058	4.00*	0.054
^{nat} Enstatite	1.616	0.058	4.00*	0.087
²⁵ Enstatite	1.617	0.058	4.00*	0.074
^{nat} MgAS_37.5_50	1.618	0.044	4.00*	1.773	0.052	4.17*	0.037
²⁵ MgAS_37.5_50	1.618	0.044	4.00*	1.772	0.052	4.17*	0.026
^{nat} MgAS_25_50	1.619	0.050	4.00*	1.767	0.072	4.27*	0.029
²⁵ MgAS_25_50	1.620	0.047	4.00*	1.771	0.071	4.27*	0.013
^{nat} MgAS_30_60	1.614	0.048	4.00*	1.775	0.052	4.20*	0.031
²⁵ MgAS_30_60	1.614	0.048	4.00*	1.774	0.052	4.20*	0.025
^{nat} MgAS_20_60	1.615	0.047	4.00*	1.775	0.065	4.22*	0.022
²⁵ MgAS_20_60	1.615	0.047	4.00*	1.775	0.065	4.22*	0.019

^aNearest-neighbor Ca–O correlations: $\bar{r}_{\text{CaO}} = 2.358(5)$ Å, $\sigma_{\text{CaO}} = 0.156(6)$ Å and $\bar{n}_{\text{Ca}}^{\text{O}} = 5.01^*$.

^bNearest-neighbor Ca–O correlations: $\bar{r}_{\text{CaO}} = 2.350(5)$ Å, $\sigma_{\text{CaO}} = 0.150(6)$ Å and $\bar{n}_{\text{Ca}}^{\text{O}} = 5.01^*$.

TABLE XI. The Mg–O peak parameters obtained from the fitted $D'_N(r)$ functions for diopside, enstatite, and the MgAS glasses. Fixed parameters are marked by an asterisk and were obtained from the measured $\Delta D'_{\text{Mg}}(r)$ functions (Table VI). The error associated with $r_{\text{MgO},i}$ is typically ± 0.004 Å ($i = 1$) or ± 0.007 Å ($i = 2$). The error associated with $\sigma_{\text{MgO},i}$ is typically ± 0.004 Å ($i = 1$) or ± 0.008 Å ($i = 2$). The weighted mean Mg–O distance \bar{r}_{MgO} was obtained from the fitted peaks by applying Eq. (18) and has a typical error of ± 0.008 Å.

Glass	First peak			Second peak			Overall \bar{r}_{MgO} (Å)	$\bar{n}_{\text{Mg}}^{\text{O}}$ (sum)
	$r_{\text{MgO},1}$ (Å)	$\sigma_{\text{MgO},1}$ (Å)	$\bar{n}_{\text{Mg},1}^{\text{O}}$	$r_{\text{MgO},2}$ (Å)	$\sigma_{\text{MgO},2}$ (Å)	$\bar{n}_{\text{Mg},2}^{\text{O}}$		
^{nat} Diopside	1.977	0.076	2.61*	2.143	0.146	1.80*	2.033	4.40*
²⁵ Diopside	1.978	0.074	2.61*	2.143	0.200	1.80*	2.031	4.40*
^{nat} Enstatite	1.984	0.084	2.59*	2.115	0.140	1.87*	2.029	4.46*
²⁵ Enstatite	1.982	0.087	2.59*	2.084	0.130	1.87*	2.016	4.46*
^{nat} MgAS_37.5_50	2.009	0.086	3.17*	2.185	0.153	1.59*	2.056	4.76*
²⁵ MgAS_37.5_50	2.010	0.086	3.17*	2.178	0.155	1.59*	2.055	4.76*
^{nat} MgAS_25_50	2.022	0.074	2.43*	2.148	0.153	2.47*	2.075	4.90*
²⁵ MgAS_25_50	2.036	0.065	2.43*	2.159	0.179	2.47*	2.086	4.90*
^{nat} MgAS_30_60	2.006	0.084	3.40*	2.212	0.105	1.36*	2.053	4.77*
²⁵ MgAS_30_60	2.009	0.081	3.40*	2.215	0.100	1.36*	2.056	4.77*
^{nat} MgAS_20_60	2.023	0.055	2.17*	2.175	0.144	2.91*	2.099	5.07*
²⁵ MgAS_20_60	2.027	0.050	2.17*	2.173	0.138	2.91*	2.100	5.07*

As noted in Sec. IV B 1, the Mg^{2+} ions in the diopside and enstatite glasses generate Si–NBO linkages and therefore adopt a network-modifying role. When alumina is introduced to the glass network, a fraction of the Mg^{2+} ions will also adopt a predominantly charge-compensating role by balancing the charge on the $[\text{AlO}_{4/2}]^-$ species.⁵⁰ Along a tie-line with constant mol. % silica, the fraction of Mg^{2+} ions that adopt a network-modifying role will therefore decrease as magnesia is replaced by alumina. The diffraction results indicate, therefore, a difference in size between the coordination environments

of Mg^{2+} ions that take a network-modifying vs a predominantly charge-compensating role. In this context, it is important to point out that, for the alumina containing glasses, a given Mg^{2+} ion may well have in its coordination sphere both Si–NBO atoms and the oxygen atoms from $[\text{AlO}_{4/2}]^-$ units and, therefore, play a dual network-modifying/charge-compensating role. The anionic charge on this Al(IV) unit may be compensated by multiple Mg^{2+} ions, each contributing a small part of the required charge and each, likewise, interacting with multiple oxygen atoms.

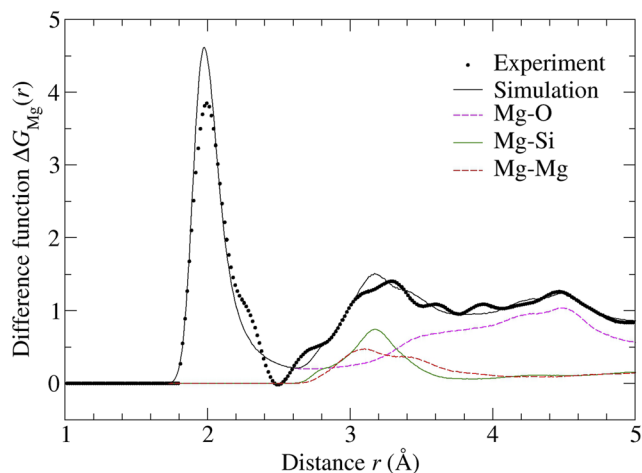


FIG. 20. The $\Delta G_{\text{Mg}}(r)$ function for enstatite glass as measured using neutron diffraction with magnesium isotope substitution (circles) or simulated using molecular dynamics (black curve).¹⁴ The contributions to the simulated function from the weighted $g_{\text{MgO}}(r)$, $g_{\text{MgSi}}(r)$, and $g_{\text{MgMg}}(r)$ functions are also given.

VI. CONCLUSIONS

Neutron powder diffraction was used to remeasure the bound coherent neutron scattering length of the magnesium isotope ^{25}Mg . The value $b_{25,\text{Mg}} = 3.720(12)$ fm was obtained, which is 2.8% larger than the literature value.¹⁸

The method of neutron diffraction with isotope substitution was used to measure the structure of diopside and enstatite composition glasses, two MgAS glasses along the 50 mol. % silica tie-line with $R = 3$ or $R = 1$, and two MgAS glasses along the 60 mol. % silica tie-line with the same R -values. As compared to the literature value for $b_{25,\text{Mg}}$,¹⁸ the new scattering length led to much improved self-consistency between the measured difference functions and their back Fourier transforms (Sec. II B). The diffraction results reveal a broad and asymmetric distribution of Mg–O nearest neighbors. In the diopside and enstatite glasses, where the Mg^{2+} ions adopt a network-modifying role, $\bar{n}_{\text{Mg}}^{\text{O}}$ is 4.40(4) and 4.46(4), respectively. As magnesia is replaced by alumina along a 50 or 60 mol. % silica tie-line, the mean Mg–O coordination number increases with the weighted Mg–O bond distance as Mg^{2+} ions also adopt the role of charge-compensators to the $[\text{AlO}_{4/2}]^-$ units, particularly in those glasses for which $R = 1$.

The glass structure was also investigated by ^{25}Mg MAS and static NMR experiments. The measured spectra could be represented by employing the Czjzek distribution model using an identical set of parameters for a given glass composition, which lends support to the strategy employed to interpret the NMR results.⁸ However, the chemical shifts obtained from unconstrained fits of the measured MAS NMR spectra appear to be more consistent with an Mg–O coordination number of six for all the investigated glasses, rather than a value in the range 4.40(4)–5.07(4) measured by diffraction. This dichotomy finds explanation in the broad distribution of electric field gradients associated with the different sites of the Mg^{2+} ions that originates from structural disorder. In the investigated glasses, the concomitant quadrupolar broadening of

the measured spectra makes it impossible to resolve the contributions from the different magnesium species, at least under the field strength (14.1 T) and spinning rate (20 kHz) employed in the MAS NMR experiments.

The present work demonstrates the power of neutron diffraction with magnesium isotope substitution to provide unambiguous site-specific information on the glass structure. In the investigated materials, it removed the uncertainties associated with overlap between (i) the Mg–O and Al–O correlations in the $D'_N(r)$ or $D'_X(r)$ functions for the MgAS glasses, (ii) the Mg–O and Ca–O correlations in the $D'_N(r)$ or $D'_X(r)$ functions for diopside glass, and (iii) the Mg–O and O–O correlations in the $D'_X(r)$ functions for all the glasses. The results thereby clarify the way in which these total pair-distribution functions should be interpreted, which will empower systematic investigations of the structure of MgAS glasses over a broader composition range to explore, e.g., the network-modifying vs charge-compensating role of the Mg^{2+} ions in more detail.

ACKNOWLEDGMENTS

We thank Kristina Brix and Ralf Kautenburger (Saarland University, Saarbrücken, Germany) for performing the ICP-MS experiments and Alain Bertoni (Grenoble, France) for help with the D4c experiments.

H.M. was supported by Corning Inc. (Agreement No. CM00002159/SA/01). R.M.D.S. was supported by the Royal Society (Grant No. RGF/EA/180060). A.Z. was supported by a Royal Society-EPSCRC Dorothy Hodgkin Research Fellowship. L.V.D.G. acknowledges funding and support from the EPSCRC Centre for Doctoral Training in Condensed Matter Physics (CDT-CMP), Grant No. EP/L015544/1, the Science and Technology Facilities Council (STFC) and Diamond Light Source Ltd. (Reference No. STU0173). P.S.S. and A.Z. are grateful to Corning Inc. for the award of Gordon S. Fulcher Distinguished Scholarships under which this work was conceived. Funding of this work by FAPESP, Project No. 2013/07793-6, is gratefully acknowledged. M.d.O., Jr. and H.E. acknowledge the National Council for Scientific and Technological Development (CNPq, Grant Nos. 311069/2020-7 and 310870/2020-8, respectively). H.D. acknowledges personal fellowship support from CNPq and Nippon Electric Glass. This research used resources of the Advanced Photon Source, a U.S. Department of Energy (DOE) Office of Science User Facility operated for the DOE Office of Science by Argonne National Laboratory under Contract No. DE-AC02-06CH11357. We acknowledge use of the Inorganic Crystal Structure Database accessed via the Chemical Database Service funded by the Engineering and Physical Sciences Research Council (EPSRC) and hosted by the Royal Society of Chemistry.

P.S.S., A.Z., R.E.Y., and B.G.A. designed the diffraction project on the glass structure. H.K. and H.E.F. designed the project to measure the neutron scattering lengths. L.C. provided the isotopically enriched samples of diopside and enstatite and the raw data sets for the enstatite glass. H.M. prepared the other glass samples and F.G. prepared the crystalline MgO samples. F.G. and H.E.F. performed the neutron powder diffraction experiments and F.G. and H.M. analyzed the results. M.d.O., Jr., H.D., and H.E. performed the NMR experiments and analyzed the results. A.Z., H.M., R.M.D.S., H.E.F.,

and P.S.S. performed the neutron diffraction experiments on the glasses and H.M., R.M.D.S., L.V.D.G., and A.Z. analyzed the results. C.J.B. performed the x-ray diffraction experiments and R.M.D.S. analyzed the results. P.S.S., M.d.O., Jr., and H.E. wrote the paper with input from all coauthors.

AUTHOR DECLARATIONS

Conflict of Interest

The authors have no conflicts to disclose.

Author Contributions

Hesameddin Mohammadi: Formal analysis (equal); Investigation (equal); Writing – review & editing (supporting). **Rita Mendes Da Silva:** Formal analysis (equal); Investigation (equal); Writing – review & editing (supporting). **Anita Zeidler:** Conceptualization (equal); Data curation (supporting); Formal analysis (equal); Funding acquisition (equal); Investigation (equal); Methodology (equal); Project administration (equal); Resources (equal); Software (equal); Supervision (equal); Writing – review & editing (supporting). **Lawrence V. D. Gammond:** Formal analysis (supporting); Investigation (supporting); Writing – review & editing (supporting). **Florian Gehlhaar:** Formal analysis (equal); Investigation (equal). **Marcos de Oliveira, Jr.:** Conceptualization (equal); Data curation (equal); Formal analysis (equal); Funding acquisition (equal); Investigation (equal); Methodology (equal); Software (equal); Visualization (equal); Writing – original draft (supporting); Writing – review & editing (supporting). **Hugo Damasceno:** Formal analysis (supporting); Investigation (supporting). **Hellmut Eckert:** Conceptualization (equal); Data curation (equal); Formal analysis (equal); Funding acquisition (equal); Investigation (equal); Methodology (equal); Project administration (equal); Resources (equal); Supervision (equal); Validation (equal); Writing – original draft (equal); Writing – review & editing (equal). **Randall E. Youngman:** Conceptualization (equal); Funding acquisition (equal). **Bruce G. Aitken:** Conceptualization (equal); Funding acquisition (equal). **Henry E. Fischer:** Conceptualization (supporting); Investigation (supporting); Supervision (equal). **Holger Kohlmann:** Conceptualization (supporting); Supervision (equal). **Laurent Cormier:** Resources (supporting). **Chris J. Benmore:** Investigation (supporting). **Philip S. Salmon:** Conceptualization (equal); Data curation (lead); Formal analysis (equal); Funding acquisition (equal); Investigation (equal); Methodology (equal); Project administration (equal); Resources (equal); Software (equal); Supervision (equal); Validation (equal); Visualization (equal); Writing – original draft (lead); Writing – review & editing (equal).

DATA AVAILABILITY

The data that support the findings of this study are openly available in University of Bath Research Data Archive at <https://doi.org/10.15125/BATH-01192>.⁷⁵ The measured neutron diffraction datasets for crystalline ²⁵MgO and ^{nat}MgO are available from Ref. 76. The measured neutron diffraction datasets for the glasses are available from Refs. 77–79.

REFERENCES

- 1 T. Yamanaka and Y. Takéuchi, *Z. Kristallogr.* **165**, 65 (1983).
- 2 S. Sasaki, K. Fujino, and Y. Takéuchi, *Proc. Jpn. Acad., Ser. B* **55**, 43 (1979).
- 3 N. Morimoto and K. Koto, *Z. Kristallogr.* **129**, 65 (1969).
- 4 P. B. Moore and J. V. Smith, *Phys. Earth Planet. Inter.* **3**, 166 (1970).
- 5 H. Xu, P. J. Heaney, P. Yu, and H. Xu, *Am. Mineral.* **100**, 2191 (2015).
- 6 E. P. Meagher, *Am. Mineral.* **60**, 218 (1975); available at http://www.minsocam.org/ammin/AM60/AM60_218.pdf.
- 7 S. J. Watts, R. G. Hill, M. D. O'Donnell, and R. V. Law, *J. Non-Cryst. Solids* **356**, 517 (2010).
- 8 M. de Oliveira, Jr., H. Damasceno, P. S. Salmon, and H. Eckert, *J. Magn. Reson. Open* **12–13**, 100067 (2022).
- 9 J. C. C. Freitas and M. E. Smith, *Annu. Rep. NMR Spectrosc.* **75**, 25 (2012).
- 10 M. Dejneka and T. J. Kiczinski, in *Springer Handbook of Glass*, edited by J. D. Musgraves, J. Hu, and L. Calvez (Springer, Cham, Switzerland, 2019), Chap. 45, pp. 1519–1551.
- 11 T. M. Gross, in *Springer Handbook of Glass*, edited by J. D. Musgraves, J. Hu, and L. Calvez (Springer, Cham, Switzerland, 2019), Chap. 8, pp. 273–296.
- 12 S. Jahn and P. A. Madden, *Phys. Earth Planet. Inter.* **162**, 129 (2007).
- 13 *Magnas under Pressure*, edited by Y. Kono and C. Sanloup (Elsevier, Amsterdam, 2018).
- 14 P. S. Salmon, G. S. Moody, Y. Ishii, K. J. Pizzey, A. Polidori, M. Salanne, A. Zeidler, M. Buscemi, H. E. Fischer, C. L. Bull, S. Klotz, R. Weber, C. J. Benmore, and S. G. MacLeod, *J. Non-Cryst. Solids: X* **3**, 100024 (2019).
- 15 S. K. Lee, J. L. Mosenfelder, S. Y. Park, A. C. Lee, and P. D. Asimow, *Proc. Natl. Acad. Sci. U. S. A.* **117**, 21938 (2020).
- 16 L. Cormier and G. J. Cuello, *Phys. Rev. B* **83**, 224204 (2011).
- 17 H. E. Fischer, A. C. Barnes, and P. S. Salmon, *Rep. Prog. Phys.* **69**, 233 (2006).
- 18 A. A. Khail, F. A. Amin, A. Al-Naimi, A. Al-Saji, G. Y. Al-Shahery, V. F. Petrunin, and M. G. Zemlyanov, *Acta Crystallogr., Sect. A: Found. Adv.* **28**, 473 (1972).
- 19 H. Ibach and H. Lüth, *Solid-State Physics*, 4th ed. (Springer, Berlin, 2009).
- 20 D. Waasmaier and A. Kirfel, *Acta Crystallogr., Sect. A: Found. Adv.* **51**, 416 (1995).
- 21 P. S. Salmon, S. Xin, and H. E. Fischer, *Phys. Rev. B* **58**, 6115 (1998).
- 22 L. V. D. Gammond, H. Auer, R. Mendes Da Silva, A. Zeidler, J. F. Ortiz-Mosquera, A. M. Nieto-Muñoz, A. C. M. Rodrigues, I. d'Aniciães Almeida Silva, H. Eckert, C. J. Benmore, and P. S. Salmon, *J. Chem. Phys.* **155**, 074501 (2021).
- 23 D. I. Grimley, A. C. Wright, and R. N. Sinclair, *J. Non-Cryst. Solids* **119**, 49 (1990).
- 24 L. Cormier and G. J. Cuello, *Geochim. Cosmochim. Acta* **122**, 498 (2013).
- 25 L. Koester, H. Rauch, and E. Seymann, *At. Data Nucl. Data Tables* **49**, 65 (1991).
- 26 V. F. Sears, *Neutron News* **3**, 26 (1992).
- 27 E. J. Catanzaro, T. J. Murphy, E. L. Garner, and W. R. Shields, *J. Res. Natl. Bur. Stand., Sect. A* **70A**, 453 (1966).
- 28 H. E. Fischer, G. J. Cuello, P. Palleau, D. Feltin, A. C. Barnes, Y. S. Badyal, and J. M. Simonson, *Appl. Phys. A* **74**, s160 (2002).
- 29 A. Zeidler, P. S. Salmon, H. E. Fischer, J. C. Neufeind, J. M. Simonson, and T. E. Markland, *J. Phys.: Condens. Matter* **24**, 284126 (2012).
- 30 J. Rodríguez-Carvajal, *Physica B* **192**, 55 (1993).
- 31 J. Rodríguez-Carvajal, FullProf suite, Institut Laue-Langevin, Grenoble, France, 2022; available at <https://www.ill.eu/sites/fullprof/php/reference.html>.
- 32 B. H. Toby and R. B. Von Dreele, *J. Appl. Cryst.* **46**, 544 (2013).
- 33 H. E. Fischer, J. M. Simonson, J. C. Neufeind, H. Lemmel, H. Rauch, A. Zeidler, and P. S. Salmon, *J. Phys.: Condens. Matter* **24**, 505105 (2012).
- 34 G. Caglioti, A. Paoletti, and F. P. Ricci, *Nucl. Instrum.* **3**, 223 (1958).
- 35 A. W. Hewat, *Nucl. Instrum. Methods* **127**, 361 (1975).
- 36 W. Bauspiess, U. Bonse, and H. Rauch, *Nucl. Instrum. Methods* **157**, 495 (1978).
- 37 A. Medek, J. S. Harwood, and L. Frydman, *J. Am. Chem. Soc.* **117**, 12779 (1995).
- 38 J.-P. Amoureux, C. Huguenard, F. Engelke, and F. Taulelle, *Chem. Phys. Lett.* **356**, 497 (2002).
- 39 D. Massiot, F. Fayon, M. Capron, I. King, S. Le Calvé, B. Alonso, J.-O. Durand, B. Bujoli, Z. Gan, and G. Hoatson, *Magn. Reson. Chem.* **40**, 70 (2002).

- ⁴⁰D. Freude and J. Haase, in *Special Applications. NMR Basic Principles and Progress*, edited by H. Pfeifer and P. Barker (Springer, Berlin, 1993), Vol. 29, pp. 1–90.
- ⁴¹J.-B. d’Espinoise de Lacaillerie, C. Fretigny, and D. Massiot, *J. Magn. Reson.* **192**, 244 (2008).
- ⁴²L. A. O’Dell, *Solid State Nucl. Magn. Reson.* **55–56**, 28 (2013).
- ⁴³H. Y. Carr and E. M. Purcell, *Phys. Rev.* **94**, 630 (1954).
- ⁴⁴S. Meiboom and D. Gill, *Rev. Sci. Instrum.* **29**, 688 (1958).
- ⁴⁵S. G. J. van Meerten, W. M. J. Franssen, and A. P. M. Kentgens, *J. Magn. Reson.* **301**, 56 (2019).
- ⁴⁶M. Bak, J. T. Rasmussen, and N. C. Nielsen, *J. Magn. Reson.* **147**, 296 (2000).
- ⁴⁷P. S. Salmon, A. Zeidler, and H. E. Fischer, *J. Appl. Cryst.* **49**, 2249 (2016).
- ⁴⁸A. P. Hammersley, *J. Appl. Cryst.* **49**, 646 (2016).
- ⁴⁹X. Qiu, J. W. Thompson, and S. J. L. Billinge, *J. Appl. Cryst.* **37**, 678 (2004).
- ⁵⁰L. V. D. Gammond, R. E. Youngman, A. Zeidler, B. G. Aitken, and P. S. Salmon, *J. Chem. Phys.* **156**, 064503 (2022).
- ⁵¹H. Eckert, *Prog. Nucl. Magn. Reson. Spectrosc.* **24**, 159 (1992).
- ⁵²H. Eckert, in *Solid-State NMR IV Methods and Applications of Solid-State NMR*, NMR Basic Principles and Progress Vol. 33, edited by B. Blümich (Springer, Berlin, 1994), pp. 125–198.
- ⁵³M. Edén, *Annu. Rep. NMR Spectrosc.* **86**, 237 (2015).
- ⁵⁴E. Gambuzzi, A. Pedone, M. C. Menziani, F. Angeli, D. Caurant, and T. Charpentier, *Geochim. Cosmochim. Acta* **125**, 170 (2014).
- ⁵⁵M. Moesgaard, R. Keding, J. Skibsted, and Y. Yue, *Chem. Mater.* **22**, 4471 (2010).
- ⁵⁶U. Werner-Zwanziger, A. L. Paterson, and J. W. Zwanziger, *J. Non-Cryst. Solids* **550**, 120383 (2020).
- ⁵⁷C. Jäger, W. Müller-Warmuth, C. Mundus, and L. van Wüllen, *J. Non-Cryst. Solids* **149**, 209 (1992).
- ⁵⁸H. Bradtmüller, T. Uesbeck, H. Eckert, T. Murata, S. Nakane, and H. Yamazaki, *J. Phys. Chem. C* **123**, 14941 (2019).
- ⁵⁹E. Lorch, *J. Phys. C: Solid State Phys.* **2**, 229 (1969).
- ⁶⁰P. S. Salmon, *J. Phys.: Condens. Matter* **18**, 11443 (2006).
- ⁶¹S. Sen, H. Maekawa, and G. N. Papatheodorou, *J. Phys. Chem. B* **113**, 15243 (2009).
- ⁶²M. C. Davis, K. J. Sanders, P. J. Grandinetti, S. J. Gaudio, and S. Sen, *J. Non-Cryst. Solids* **357**, 2787 (2011).
- ⁶³J. Schneider, V. R. Mastelaro, H. Panepucci, and E. D. Zanotto, *J. Non-Cryst. Solids* **273**, 8 (2000).
- ⁶⁴J. R. Clark, D. E. Appleman, and J. J. Papike, in *Mineralogical Society of America Special Paper Number Two: Pyroxenes and Amphiboles: Crystal Chemistry and Phase Petrology*, edited by J. J. Papike (Mineralogical Society of America, Menasha, WI, 1969), pp. 31–50; available at http://www.minsocam.org/MSA/OpenAccess_Publications/MSA_SP_2/MSA_SP2_031-050.pdf.
- ⁶⁵S. Kroeker and J. F. Stebbins, *Am. Mineral.* **85**, 1459 (2000).
- ⁶⁶S. Kroeker, P. S. Neuhoff, and J. F. Stebbins, *J. Non-Cryst. Solids* **293–295**, 440 (2001).
- ⁶⁷N. Bisbrouck, M. Bertani, F. Angeli, T. Charpentier, D. de Ligny, J. M. Delaye, S. Gin, and M. Micoulaut, *J. Am. Ceram. Soc.* **104**, 4518 (2021).
- ⁶⁸K. Shimoda, Y. Tobu, M. Hatakeyama, T. Nemoto, and K. Saito, *Am. Mineral.* **92**, 695 (2007).
- ⁶⁹K. Shimoda, T. Nemoto, and K. Saito, *J. Phys. Chem. B* **112**, 6747 (2008).
- ⁷⁰M. Guignard and L. Cormier, *Chem. Geol.* **256**, 111 (2008).
- ⁷¹P. Zhang, P. J. Grandinetti, and J. F. Stebbins, *J. Phys. Chem. B* **101**, 4004 (1997).
- ⁷²D. C. Kaseman, A. Retsinas, A. G. Kalampounias, G. N. Papatheodorou, and S. Sen, *J. Phys. Chem. B* **119**, 8440 (2015).
- ⁷³D. R. Neuville and P. Richet, *Geochim. Cosmochim. Acta* **55**, 1011 (1991).
- ⁷⁴D. R. Neuville and C. Le Losq, *Rev. Mineral. Geochem.* **87**, 105 (2022).
- ⁷⁵P. S. Salmon and A. Zeidler, Structure of diopside, enstatite and magnesium aluminosilicate glasses: A joint approach using neutron and x-ray diffraction and solid-state NMR, University of Bath Research Data Archive, 2022, <https://doi.org/10.15125/BATH-01192>.
- ⁷⁶F. Gehlhaar, H. E. Fischer, T. Hansen, and H. Kohlmann, Accurate neutron scattering lengths of Sm- and Nd-isotopes, Institut Laue-Langevin, Grenoble, France, 2021, <https://doi.ill.fr/10.5291/ILL-DATA.1-10-50>.
- ⁷⁷P. S. Salmon, H. Eckert, H. E. Fischer, L. V. D. Gammond, R. Mendes Da Silva, H. Mohammadi, and A. Zeidler, Structural change in phosphate-based glassy precursors to superionic conducting glass-ceramic electrolytes, Institut Laue-Langevin, Grenoble, France 2019, <https://doi.org/10.5291/ILL-DATA.6-05-1009>.
- ⁷⁸P. S. Salmon, B. G. Aitken, H. E. Fischer, L. V. D. Gammond, R. Mendes Da Silva, H. Mohammadi, and A. Zeidler, Structure of magnesium aluminosilicate glass by neutron diffraction with isotope substitution, Institut Laue-Langevin, Grenoble, France, 2019, <https://doi.org/10.5291/ILL-DATA.6-05-1002>.
- ⁷⁹E. Girón Lange, F. H. Cova, G. J. Cuello, H. Mohammadi, P. S. Salmon, G. Vaughan, and A. Zeidler, Structure of aluminosilicate glasses by NDIS, Institut Laue-Langevin, Grenoble, France, 2021, <https://doi.org/10.5291/ILL-DATA.INTER-562>.
- ⁸⁰A. C. Hannon, private communication (2022).